nature nanotechnology

Article

https://doi.org/10.1038/s41565-024-01784-1

A cuproptosis nanocapsule for cancer radiotherapy

Received: 25 September 2023

Accepted: 8 August 2024

You Liao[1,2,4], Dongmei Wang[1,2,4], Chenglu Gu[1,2], Xue Wang[1,2], Shuang Zhu[1,2], Ziye Zheng[3], Fuquan Zhang[3], Junfang Yan[3] ✉ & Zhanjun Gu[1,2] ✉

Residual tumours that persist after radiotherapy often develop acquired radiation resistance, increasing the risk of recurrence and metastasis while providing obstacles to re-irradiation. Using samples from patients and experimental mice, we discovered that FDX1 and LIAS, key regulators of cuproptosis, were up-regulated in residual tumours following radiotherapy, conferring the increased sensitivity to cuproptosis. Therefore, we proposed a novel radiosensitization strategy focused on cuproptosis, using a copper-containing nanocapsule-like polyoxometalate as a paradigm. In an initial demonstration, we showed that the nanocapsule released copper ions in a controlled manner upon exposure to ionizing radiation. Furthermore, radiation-triggered cuproptosis overcame acquired radiation resistance even at clinically relevant radiation doses and activated a robust abscopal effect, with a 40% cure rate in both radioresistant and re-irradiation tumour models. Collectively, targeting cuproptosis is a compelling strategy for addressing acquired radiation resistance, optimizing the local antitumour effects of radiotherapy while simultaneously activating systemic antitumour immunity.

Cancer ranks as a leading cause of premature death worldwide, despite major advances in clinical anti-cancer therapies[1]. As a clinical therapy for over a century, radiotherapy has been used for the curative or palliative treatment of localized tumours or oligometastasis and is included in the treatment of more than 50% of patients[2–4]. Nevertheless, clinically fractionated radiotherapy triggers the development of acquired radiation resistance in the residual tumours[5]. Acquired radiation resistance confers residual tumours with the ability to escape the effects of radiation therapy, thereby increasing the risk of locoregional recurrence. Incremental patients with locoregional recurrent tumours following primary radiotherapy are treated with ionizing radiation (IR) to a previously irradiated lesion of the body, commonly referred to as re-irradiation[6]. Due to the increased radiation resistance of recurrent tumours, high-dose radiation is required to achieve the desired re-irradiation effect. However, the tolerance of normal tissues to radiation doses is often limited especially in cases with an overlapped radiation field or a short interval between re-irradiation and primary irradiation, which restricts the delivery of high re-irradiation doses. For instance, a considerable percentage of breast cancer patients, exceeding 50%, manifest acute toxicity reactions following re-irradiation[7]; up to 21% of lung cancer patients experience severe lung toxicity, often presenting as radiation pneumonitis, requiring oxygen supply or respiratory support, following re-irradiation[8]. In local recurrent gliomas, re-irradiation may lead to elevated rates of toxicity occurrence and more severe adverse reactions, including necrosis, cognitive disorder and secondary malignancies[9]. Thus, the mismatch between the acquired radioresistance of tumours and the radiation tolerance limits of adjacent normal tissues or organs severely

---

[1]CAS Key Laboratory for Biomedical Effects of Nanomaterials and Nanosafety, Institute of High Energy Physics, Chinese Academy of Sciences, Beijing, China. [2]College of Materials Science and Optoelectronic Technology, University of Chinese Academy of Sciences, Beijing, China. [3]Department of Radiation Oncology, Peking Union Medical College Hospital, Chinese Academy of Medical Sciences and Peking Union Medical College, Beijing, China. [4]These authors contributed equally: You Liao, Dongmei Wang. ✉e-mail: yanjunfang@pumch.cn; zjgu@ihep.ac.cn

restricts the clinical benefits for patients undergoing re-irradiation. Despite enormous effort in advances of precise radiation techniques such as intensity-modulated radiotherapy[10], volumetric-modulated arc therapy[11] or brachytherapy[12], the development of radiation sensitization strategies for tumours with acquired radioresistance remains a daunting challenge.

The clinical mission of radiotherapy is to prevent the proliferation of tumour cells and initiate their death[5,13,14]. The emergence of newly identified cell death mechanisms presents opportunities for the development of advanced radiation sensitization approaches. For example, the clarification of necroptosis[15], autophagy[16], ferroptosis[17], pyroptosis[18] and other emerging cell death mechanisms has provided new insights into radiation sensitization[19]. Cuproptosis, a copper-dependent cell death, is a newly identified mechanism of programmed death characterized by the dysregulation of copper metabolism within cells[20]. Exploring new radiation sensitization strategies based on cuproptosis mechanisms holds promise for addressing the challenges of the tumour that has acquired radioresistance. Here we describe the discovery of cuproptosis-oriented radiosensitizing potential that is diversely erected in the residual lesion of both human and experimental tumours post-primary radiotherapy, involving the up-regulation of ferredoxin 1 (FDX1) and lipoyl synthase (LIAS) proteins. Cuproptosis occurs via proteotoxic stress induced by copper-promoted aggregation of lipoylated proteins and instability of Fe–S cluster proteins in the tricarboxylic acid (TCA) cycle[20,21]. Mechanistically, both FDX1 and LIAS play key roles in promoting cuproptosis[20]. First, as key regulators of protein lipoylation, FDX1 and LIAS participate in the regulation of protein lipoylation including dihydrolipoamide *S*-acetyltransferase (DLAT). The lipoylated proteins directly bind to copper ions and form the oligomers. Second, FDX1 reduces Cu^{2+} to the more cytotoxic Cu^{+}, leading to the destabilization of Fe–S cluster proteins. Notably, these clues highlight that up-regulated FDX1 and LIAS in residual tumours following primary radiotherapy strongly predict increased sensitivity to cuproptosis, providing an opportunity to overcome the radiation resistance of residual tumours following primary radiotherapy.

Here we sought to propose a cuproptosis-oriented radiosensitization strategy for challenging radioresistant tumours. To test this idea, the copper-containing sandwich polyoxometalate $Na_{10}[(PW_9O_{34})_2Cu_4(H_2O)_2]\cdot 18H_2O$ (PWCu) was designed as controlled copper nanocapsules. The nanocapsule-like structure was formed by two B-α-isomeric $[PW_9O_{34}]^{9-}$ polyoxoanions and four coplanar CuO_6 octahedra encapsulated between them, where the CuO_6 octahedra with ultra-high specific surface area were readily reduced by reductive products of water radiolysis. When activated by X-ray irradiation, precisely released Cu^{+} ions from the nanocapsule bind directly to the lipoylated proteins of the TCA cycle, resulting in cuproptosis characterized by Fe–S cluster protein loss and lipoylated protein aggregation. We found that radiation-triggered cuproptosis mediated by this copper nanocapsule could reverse radiation resistance and strengthen the abscopal effect in metastatic tumours via improving tumour immunogenicity. As a result, the cuproptosis nanocapsules achieved striking therapeutic efficacy on both local tumours and distant metastases in acquired radioresistant murine breast 4T1-R (R denotes radioresistance) and re-irradiation 4T1 tumour models. Our cuproptosis-oriented radiosensitizer based on copper-containing nanocapsule-like polyoxometalate is therefore a promising drug candidate for re-irradiation; our application of this strategy indicates that cuproptosis can induce robust antitumour immunity to optimize the abscopal effects of radiotherapy.

Results

Up-regulation of FDX1 and LIAS in cancer cell post-radiation

Excessive copper ions interacting with lipoylated proteins of the TCA cycle trigger cuproptosis, with FDX1 and LIAS regulating protein lipoylation and indicating susceptibility to cuproptosis[20–23]. To investigate cuproptosis-related features in residual tumours post-fractionated irradiation, we assessed FDX1 and LIAS expression in clinical human cervical carcinoma (CCA) lesions before and after external beam radiation therapy (Supplementary Fig. 1). Interestingly, FDX1 and LIAS were up-regulated in residual human CCA lesions following external beam radiation therapy of 1.8 Gy × 20 (Fig. 1a,b). To further substantiate the up-regulation of FDX1 and LIAS in tumours following fractionated irradiation, we simulated the process of fractionated irradiation in mouse tumour models (Supplementary Fig. 2a). Following an initial fractionated irradiation of 4 Gy × 5, subsequent re-irradiation of 2 Gy × 3 was ineffective in suppressing residual CT26 tumours (Supplementary Fig. 2), indicating acquired radioresistance in these tumours. The local recurrent tumour model following fractionated irradiation can serve as a research platform for re-irradiation. Next, we evaluated the expression of FDX1 and LIAS in experimental cognate mouse tumours (4T1, CT26, B16-F10 and Hepa 1-6) and mice-bearing xenografted human tumours (HeLa, A549, MDA-MB-231 and HCT116) pre- and post-fractionated irradiation (Extended Data Fig. 1a). Consistently, the expression levels of FDX1 and LIAS in these residual tumours were significantly up-regulated after fractionated irradiation of 4 Gy × 5 (Fig. 1c,d and Extended Data Fig. 1b–d). Therefore, we hypothesized that cancer cells with acquired radioresistance might exhibit heightened sensitivity to cuproptosis. To test this idea, we constructed radioresistant cell lines through continuous fractionated irradiation to gather cell-level clues (Fig. 1e)[24]. Cell lines irradiated with 2 Gy × 20 exhibited acquired radioresistance, as evidenced by increased clonogenic survival compared to their parental cells (Fig. 1f)[25]. Consistent with residual tumours, the radiation-resistant cells exhibited increased expression of FDX1 and LIAS, predicting a heightened sensitivity to cuproptosis (Fig. 1g). To validate this, we assessed the cuproptosis sensitivity indicated by the cytotoxicity of the elesclomol–Cu pulse treatment, a standard cuproptosis induction method[20]. Also of interest, radiation-resistant cells exhibited increased susceptibility to cuproptosis compared to their parental cells (Fig. 1h). These findings offer initial insights into the potential relationship between acquired radioresistance and the susceptibility of residual tumours to cuproptosis following fractionated irradiation.

Preparation and characterization of PWCu nanocapsules

Given the findings described above, we hypothesized that precise induction of cuproptosis could be a viable strategy to improve the therapeutic effectiveness of radiotherapy in radiation-resistant tumour cells. As proof of concept, the copper-containing polyoxometalate PWCu was synthesized from $CuCl_2\cdot 2H_2O$ and thermalized $Na_8HPW_9O_{34}\cdot 19H_2O$ (PW_9) in a mildly heated aqueous solution (Supplementary Fig. 3a). Using this straightforward synthesis method, a single batch yielded up to several hundred grams (286.1 g) of PWCu polyoxometalate (Supplementary Fig. 3b). This large-scale synthesis is beneficial for potential clinical translation[26]. The PWCu polyoxometalate was a triclinic structure with a $P1$ space group, as confirmed by X-ray single-crystal diffraction analysis (Supplementary Table 1). The nanocapsule-like structure of the $[(PW_9O_{34})_2Cu_4(H_2O)_2]^{10-}$ polyoxoanion consisted of two B-α-isomeric PW_9 polyoxoanions with four coplanar CuO_6 octahedra positioned between them, exhibiting ultra-small particle sizes of 1–1.6 nm (Fig. 2a and Supplementary Fig. 3c). Furthermore, PWCu nanocapsules were readily soluble in various aqueous solutions, indicating their potential for effective biological use (Supplementary Fig. 3g). Importantly, the ultra-small size and unique nanocapsule-like structure of PWCu enabled an ultra-high exposure rate of the CuO_6 octahedra. In the PWCu nanocapsule, the chemical valence of Cu was identified as +2 from the X-ray photoelectron spectrum, whereas the Cu^{2+} ions could accept electrons and undergo a reduction reaction due to the relatively low reduction potential of Cu^{2+}/Cu^{+} of 0.16 V versus a standard hydrogen electrode (Supplementary Fig. 3d–f)[27]. In radiotherapy, IR can induce the radiolysis of water in the physiological environment, generating a substantial

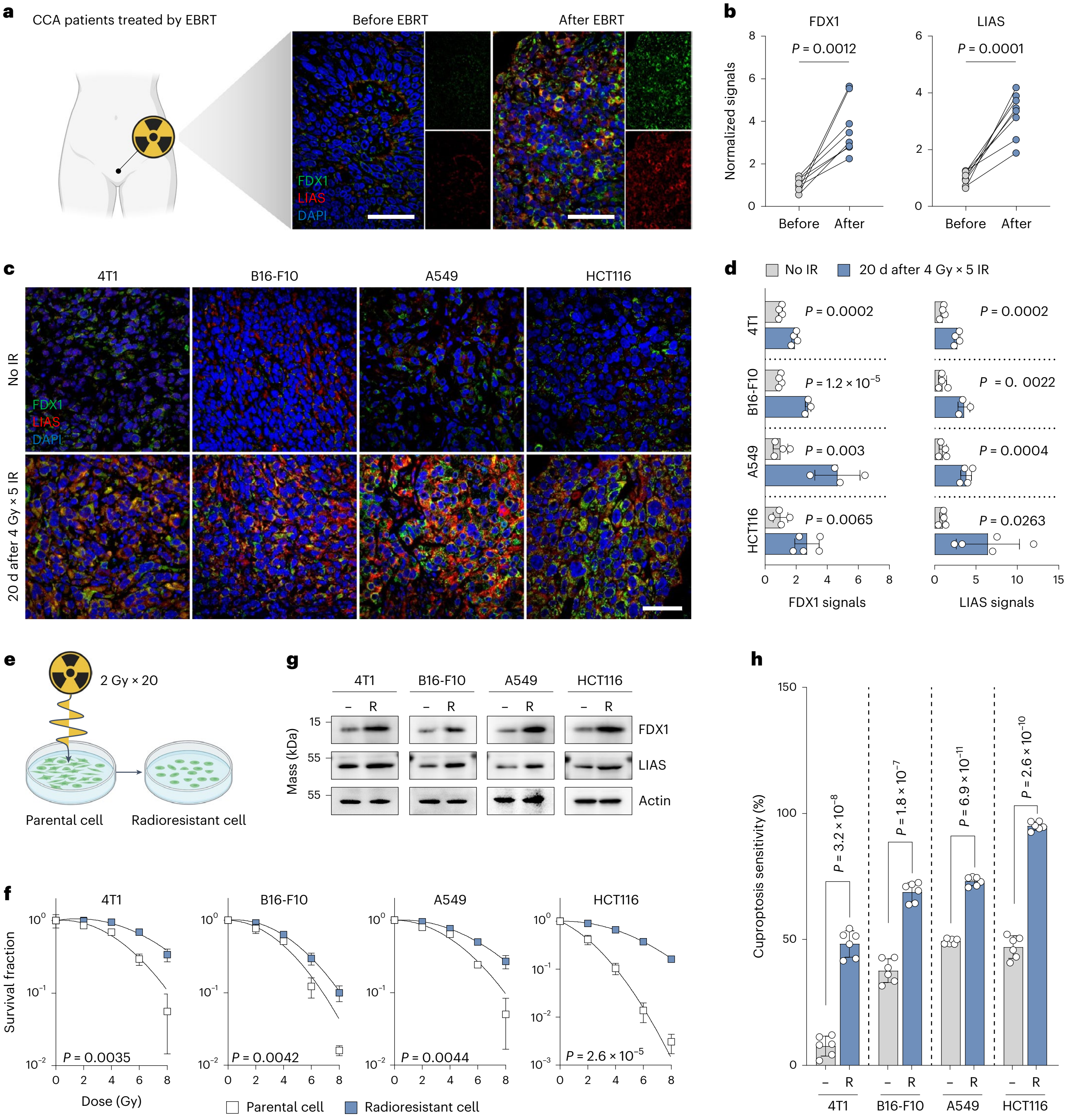

Fig. 1 | Up-regulation of FDX1 and LIAS in tumour cells after X-ray irradiation. **a**, Schematic illustration of CCA patients treated by external beam radiation therapy (EBRT) and representative confocal images (scale bars, 50 μm) of human CCA lesions (green, FDX1; red, LIAS; blue, nuclei; DAPI, 4′,6-diamidino-2-phenylindole). **b**, Normalized fluorescence signals of FDX1 and LIAS; *n* = 8 independent CCA patients. **c**, Confocal images (scale bar, 50 μm) of tumours from mouse models before and after X-ray irradiation (green, FDX1; red, LIAS; blue, nuclei). **d**, Normalized fluorescence signals of FDX1 and LIAS (*n* = 4 mice for unirradiated 4T1 tumours; *n* = 4 mice for irradiated 4T1 tumours; *n* = 4 mice for unirradiated B16-F10 tumours; *n* = 3 mice for irradiated B16-F10 tumours; *n* = 4 mice for unirradiated A549 tumours; *n* = 4 mice for irradiated A549 tumours; *n* = 4 mice for unirradiated HCT116 tumours; *n* = 5 mice for irradiated HCT116 tumours). **e**, Schematic representation of the experimental set-up used to obtain radioresistant cells by fractionated radiotherapy (2 Gy per fraction). **f**, Clonogenic survival of parental and radioresistant cells; *n* = 3 biological replicates. **g**, Immunoblot analysis of FDX1 and LIAS expressions in parental (−) and radioresistant (R) cells. **h**, Cuproptosis sensitivity (cell killing efficacy) of cells to elesclomol–Cu pulse treatment; *n* = 6 biological replicates. In **d**, **f** and **h**, data are represented as mean ± standard deviation (s.d.). *P* values were calculated by two-tailed paired *t*-test (**b**) and two-tailed unpaired *t*-test (**d**, **f** at 8 Gy and **h**). Panels **a** and **e** created with BioRender.com.

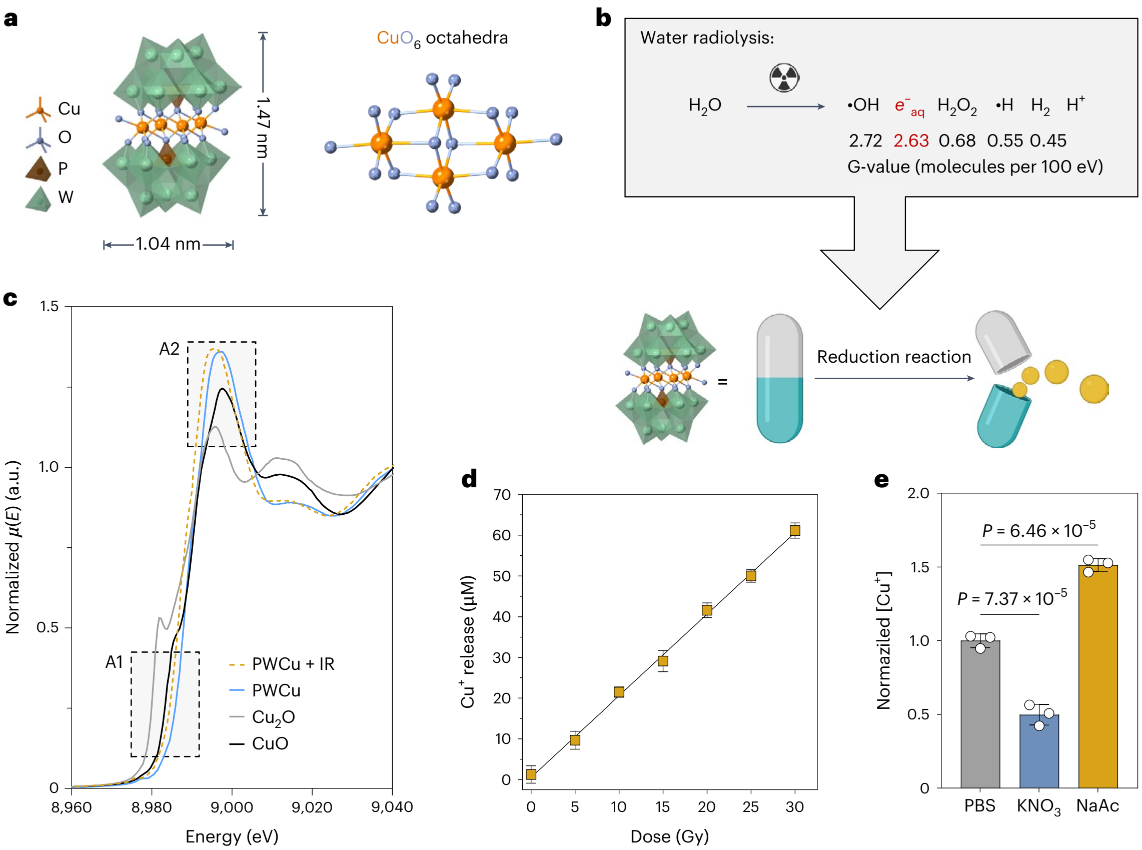

Fig. 2 | Characterization of PWCu nanocapsules. a, Structure of PWCu nanocapsules (left) and four coplanar CuO_6 octahedra (right). **b**, Schematic diagram illustrating the reaction between PWCu nanocapsules and water radiolysis products such as hydrated electrons (e^-_{aq}), leading to the release of Cu^+ ions. *G*-value, radiation chemical yield. **c**, Cu K-edge X-ray absorption near edge structure (XANES) profiles of IR-irradiated PWCu, PWCu, Cu_2O and CuO. μ, the absorption coefficient; *E*, X-ray energy; A1, the absorption edge; A2, the white line peak. **d**, IR-triggered Cu^+ ion release from PWCu nanocapsules detected by the specific agent neocuproine; $n = 3$ independent experiments. **e**, Normalized concentration of Cu^+ ions released from PWCu nanocapsules treated with KNO_3 (e^-_{aq} quencher) or NaAc (hydroxyl radical quencher) after IR irradiation, respectively, normalized to the standard phosphate-buffered saline (PBS); $n = 3$ independent experiments. Data in **d** and **e** are represented as mean ± s.d. *P* values were calculated by one-way analysis of variance (ANOVA) followed by Tukey's multiple comparison test (**e**). Panel **b** created with BioRender.com.

quantity of radiolysis products such as hydrogen atoms (•H), hydroxyl radicals (•OH) and hydrated electrons (e^-_{aq}). In this case, e^-_{aq} has high reactivity with a reduction potential at −2.87 V versus the standard hydrogen electrode[28–30]. Therefore, the CuO_6 octahedra within PWCu nanocapsules could exhibit high reactivity with the radiolysis product of water, enabling the radiation-controlled release of copper ions (Fig. 2b). To test this idea, we used a synchrotron-radiation-based X-ray absorption fine structure (XAFS) technique to examine alterations in the chemical valence of Cu within the nanocapsules in solution following X-ray irradiation. Notably, the absorption edge (A1) and the white line peak (A2) shifted towards the reduced Cu^+ species, indicating a reaction between the initial Cu^{2+} and the reductive radiolysis product (Fig. 2c). Furthermore, the controlled release of Cu^+ ions from PWCu nanocapsules upon IR exposure was validated using neocuproine, a specific reagent for Cu^+ detection (Supplementary Fig. 4)[28,31,32]. The PWCu nanocapsule exhibited a linear increase in the generation of Cu^+ ions with IR doses (Fig. 2d and Supplementary Fig. 4c). To verify the mechanism of radiation-induced conversion of Cu^{2+} to Cu^+, the quench agents for •OH (sodium acetate (NaAc)) and e^-_{aq} (KNO_3) were incubated with PWCu during IR irradiation. In comparison with the control group, the addition of NaAc promoted the production of Cu^+ ions. This can be attributed to the quenching of the oxidizing radiolysis product •OH by NaAc, promoting the production of extra e^-_{aq} (ref. 30). By contrast, the addition of KNO_3 significantly restrained the generation of Cu^+ ions (Fig. 2e). These results demonstrate the controlled release of Cu^+ ions from PWCu nanocapsules upon IR irradiation, providing a promising option for the precise induction of copper-dependent cell death.

PWCu-mediated radiosensitization and mechanisms in vitro

Before examining the radiosensitization, the acute cytotoxicity and cellular internalization of PWCu nanocapsules were evaluated. No cytotoxicity was observed in several human normal tissue cell lines dosed with PWCu nanocapsules (Supplementary Fig. 5a). PWCu nanocapsules exhibited higher cellular internalization compared to $CuCl_2$ (Supplementary Fig. 5b). Next, radiation-triggered intracellular release of Cu^+ ions from PWCu nanocapsules was confirmed by the Coppersensor-1 probe, which emitted fluorescence upon binding specifically to Cu^+ ions (Fig. 3a)[33]. By contrast, standalone PWCu nanocapsules or IR irradiation did not increase the intracellular Cu^+ level (Supplementary Fig. 5c,d). Subsequently, we confirmed the radiosensitization of PWCu nanocapsules. Both PW_9 and $CuCl_2$, the raw components of PWCu nanocapsules, exhibited negligible impact on cytotoxicity under radiation exposure. By contrast, PWCu nanocapsules showed concentration-dependent cytotoxicity with a half-maximal inhibitory concentration (IC_{50}) value of 1.02 μM upon radiation exposure (Fig. 3b). Furthermore, PWCu demonstrated a potent anti-proliferation ability evaluated by clonogenic survival assays under radiation exposure with a radiation enhancement factor of 1.88, whereas PW_9 or $CuCl_2$ did not (Fig. 3c). These results suggest that PWCu nanocapsules can release cytotoxic Cu^+ ions in a

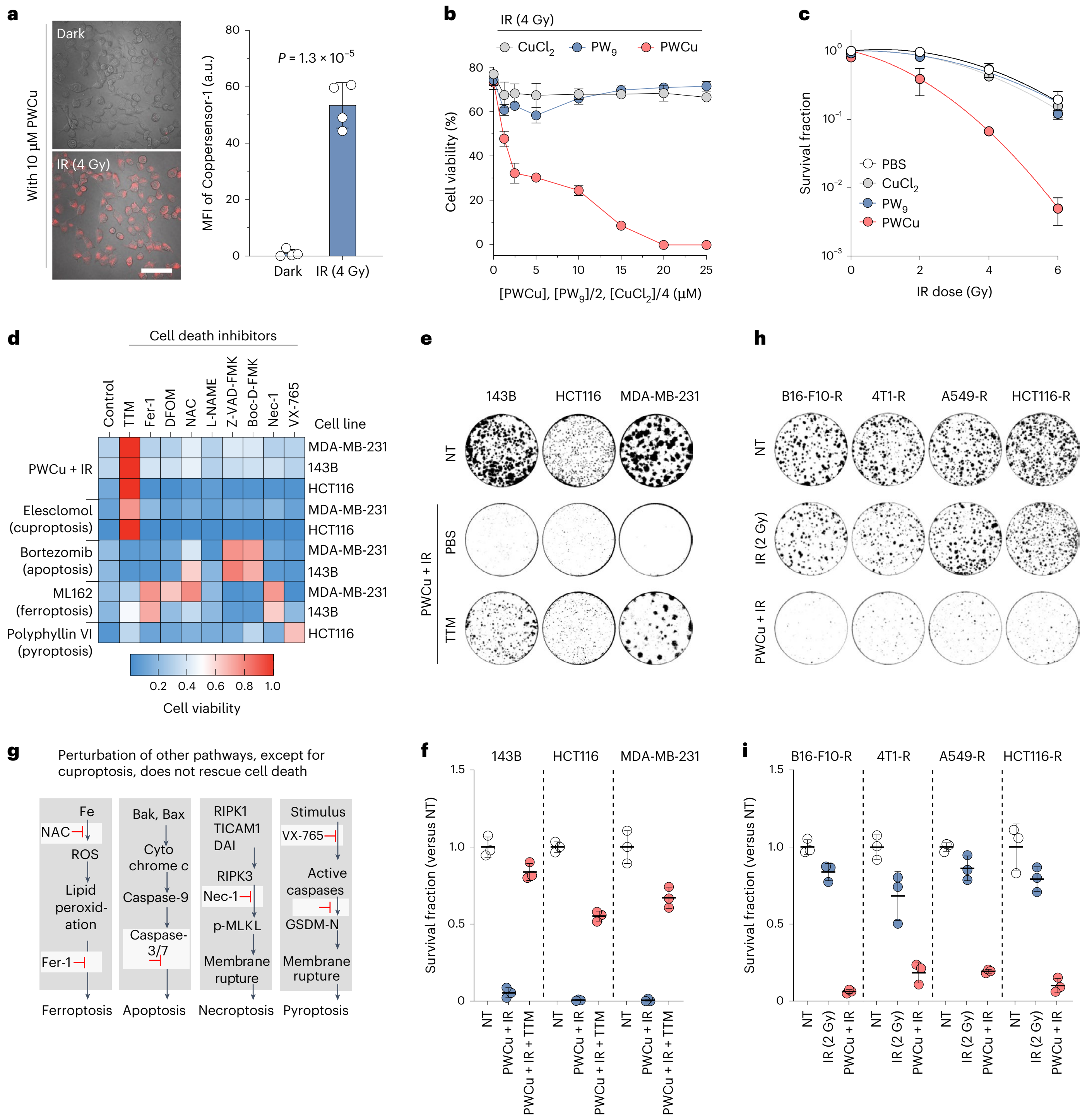

Fig. 3 | PWCu-mediated radiosensitization overcomes acquired radiation resistance via cuproptosis. a, Representative confocal images of Coppersensor-1 (a Cu$^+$-specific fluorescent probe) in 4T1 cells and mean fluorescence intensity (MFI); scale bar, 50 μm; *n* = 4 fields. **b**, Cytotoxicity of PWCu, PW$_9$ or CuCl$_2$ upon X-ray irradiation at a dose of 4 Gy on 4T1 cells; *n* = 6 replicates. **c**, Clonogenic assays to evaluate the radiosensitization of PWCu, PW$_9$ or CuCl$_2$ on 4T1 cells upon X-ray irradiation; *n* = 3 biological replicates. **d**, Heat map of cell viability incubated with 20 μM TTM, 10 μM Fer-1, 60 μM DFOM, 1 mM NAC, 20 μM L-NAME, 10 μM Z-VAD-FMK, 50 μM Boc-D-FMK, 20 μM Nec-1 or 1 μM VX-765 and treated with 5 μM PWCu plus 2 Gy IR, 30 nM elesclomol–CuCl$_2$ (1:1), 50 nM bortezomib, 1 μM ML162 or 10 μM polyphyllin VI, for 60 h (average of three replicates). The colour bar refers to cell viability where blue indicates significant cell death and red indicates good cell viability. **e**, Representative images of clonogenic survival assays of 143B, HCT116 or MDA-MB-231 cells that were pretreated with 10 μM PWCu, or 10 μM PWCu plus 20 μM TTM for 6 h followed by IR exposure at a dose of 4 Gy. NT, no treatment. **f**, Survival fractions of the cells in **e**; *n* = 3 biological replicates. **g**, Diagram of ferroptosis, apoptosis, necroptosis and pyroptosis. Inhibited pathways are indicated by the inhibition arrows. ROS, reactive oxygen species; Bak, BCL2 antagonist/killer; Bax, BCL2 associated X; RIPK, receptor-interacting protein kinase; TICAM1, toll like receptor adaptor molecule 1; DAI, DNA-dependent activator of IFN-regulatory factors; p-MLKL, phosphorylated mixed lineage kinase domain-like protein; GSDM-N, gasdermin N-terminal domain. **h**, Representative images of clonogenic survival assays of B16-F10-R, 4T1-R, A549-R or HCT116-R cells that were pretreated with or without 10 μM PWCu for 6 h followed by IR exposure of 2 Gy. **i**, Survival fractions of the radioresistant cells in **h**; *n* = 3 biological replicates. Data in **a**–**c**, **f** and **i** are shown as mean ± s.d. The *P* value was calculated by a two-tailed unpaired *t*-test (**a**).

radiation-controlled manner within cancer cells, thereby achieving radiation sensitization.

Next, the mechanism of PWCu-mediated radiosensitization was investigated. Diverse cell death inhibitors—including the ferroptosis inhibitor ferrostatin-1 (Fer-1) and deferoxamine mesylate (DFOM), the oxidative stress inhibitor *N*-acetyl cysteine (NAC), the apoptosis inhibitors carbobenzoxy-valyl-alanyl-aspartyl-[*O*-methyl]-fluoromethylketone (Z-VAD-FMK) and methyl 5-fluoro-3-[(2-methylpropan-2-yl)oxycarbonylamino]-4-oxopentanoate (Boc-D-FMK) and the necroptosis inhibitor necrostatin-1 (Nec-1)—presented no rescue effects on PWCu-induced cell death upon IR irradiation (Fig. 3d)[20,34]. By contrast, the copper chelator tetrathiomolybdate (TTM) reversed the cell death, suggesting that cuproptosis was the dominant form of cell death (Fig. 3d)[20,35,36]. Furthermore, TTM reversed the decrease in clonogenic survival caused by PWCu plus IR treatment (Fig. 3e,f). These results demonstrate that the combination of PWCu and IR induces cuproptosis in cancer cells, rather than other forms of programmed cell death (Fig. 3g)[20]. Encouraged by the precise induction of cuproptosis, we explored the radiosensitizing potential of PWCu nanocapsules in radiation-resistant tumour cells. Interestingly, PWCu nanocapsules demonstrated potent cytotoxicity against radiation-resistant tumour cells even at a low IR dose of 2 Gy (Fig. 3h,i). Taken together, PWCu nanocapsules can precisely induce cuproptosis under IR irradiation, overcoming the acquired radioresistance.

Subsequently, we evaluated the nature of the cell death of dying radiation-resistant tumour cells induced by PWCu nanocapsules under IR exposure. Considering that cuproptosis primarily affects the TCA cycle in the mitochondrial respiratory process, we first evaluated whether PWCu plus IR treatment caused mitochondrial damage[37,38]. PWCu or IR alone did not significantly reduce the mitochondrial membrane potential as indicated by tetramethylrhodamine, ethyl ester (TMRE) fluorescence, while PWCu plus IR caused significant mitochondrial damage that could be reversed by TTM (Supplementary Figs. 6a,b and 7)[39]. Furthermore, mitochondrial shrinkage and reduced cristae, indicative of substantial damage, were observed in cells following PWCu plus IR treatment (Fig. 4a,b and Supplementary Fig. 6c,d). Consistently, the spare respiratory capacity was markedly decreased after the PWCu plus IR treatment, implying severe disruption of the mitochondrial TCA cycle (Supplementary Fig. 8). Next, we evaluated the expression of cuproptosis-related proteins after different treatments. Consistent with the cuproptosis-positive group (elesclomol–Cu), PWCu plus IR treatment induced DLAT aggregation (Fig. 4c,d and Supplementary Fig. 9), loss of lipoylated TCA cycle proteins lip-DLAT and lip-DLST (Supplementary Fig. 10), down-regulation of Fe–S cluster proteins (Fig. 4e and Supplementary Fig. 10) and increased heat shock protein 70 protein (HSP70) levels (Fig. 4e)[20,40–42]. By contrast, PWCu or IR alone did not elicit the cuproptosis-associated changes. Indeed, HSP70 is implicated in immunogenic cell death and may stimulate antitumour immune responses[43–45]. Inspired by this observation, we investigated other damage-associated molecular patterns (DAMPs) including calreticulin (CRT) and high mobility group box 1 (HMGB1) in tumour cells treated with PWCu plus IR. Notably, we detected significant CRT exposure and HMGB1 release in tumour cells treated with PWCu plus IR (Fig. 4f–j). These results indicate that cuproptosis induced by PWCu nanocapsules plus IR is accompanied by DAMP release, potentially enhancing antitumour immunity (Fig. 4k).

PWCu-mediated radiosensitization and immune activation

Prior to assessing radiosensitization efficacy in vivo, the biocompatibility of PWCu nanocapsules was validated in BALB/c mice via daily intravenous injections with three doses, with stable body weights and haematological parameters (Supplementary Fig. 11)[46,47]. No major organ damage was observed (Supplementary Fig. 12). The negligible haemolysis rate substantiated the suitability of PWCu nanocapsules for injectable drug administration (Supplementary Fig. 13). Given the localized nature of radiotherapy, we administered PWCu nanocapsules via intratumoural injection. Following the intratumoural injection, PWCu nanocapsules demonstrated a favourable spatial distribution (Extended Data Fig. 2). Importantly, PWCu plus IR treatment did not adversely affect body weights or haematological parameters (Supplementary Fig. 14). Furthermore, Cu was excretable via faeces, did not accumulate in normal tissues and had negligible side effects (Supplementary Figs. 15 and 16).

Next, we constructed a radiation-resistant tumour model by implanting 4T1-R cells (Supplementary Fig. 17a). In the 4T1-R tumour model, 2 Gy × 3 IR resulted in a 13% tumour growth inhibition rate, significantly lower than the 46% tumour growth inhibition rate in the 4T1 tumour model ($P = 0.0058$; Fig. 5a,b and Supplementary Fig. 17b–d), indicating the acquired radioresistance in 4T1-R tumours. Consistent with the aforementioned results (Fig. 1), FDX1 and LIAS were significantly up-regulated in radiation-resistant tumours, indicating heightened cuproptosis susceptibility (Fig. 5c,d). We further assessed the radiosensitization and the antitumour immune effects of PWCu nanocapsules in the bilateral flank 4T1-R tumour model (Fig. 5e). Local PWCu nanocapsule injection followed by low-dose IR irradiation resulted in complete elimination of the treated primary tumours (Fig. 5f,g). This potent local radiosensitization was further validated in the orthotopic 4T1-R tumour model (Extended Data Fig. 3a). Notably, PWCu nanocapsules demonstrated superior radiosensitizing effects over the representative HfO_2 nano-radioenhancer, highlighting the potential of cuproptosis-based radiosensitizers (Extended Data Fig. 3b–e). Furthermore, PWCu plus IR treatment induced the regression or elimination of the untreated distant tumours, contrasting with the negligible impact of IR alone on both distant and primary tumours (Fig. 5f,g). To assess adaptive immune activation, $CD8^+$ T cell depletion with αCD8 antibody was performed concurrently with the PWCu plus IR treatment[48]. The αCD8 treatment led to the loss of antitumour efficacy in primary tumours and the absence of the abscopal effect in distant tumours, verifying the adaptive antitumour immunity activated by the PWCu plus IR treatment (Fig. 5f,g). Next, we analysed the cell death characteristics in primary tumours and the immune infiltration in distant tumours. The PWCu plus IR treatment induced cuproptosis in the primary tumour, with characteristics of DLAT aggregation, loss of lipoylated proteins lip-DLAT and lip-DLST and the down-regulation of Fe–S cluster proteins (Supplementary Figs. 18 and 19). Importantly, the PWCu plus IR treatment significantly elevated the DAMP levels in primary tumours, with HSP70 up-regulation, CRT exposure and HMGB1 release (Supplementary Fig. 20). These elevated DAMPs accompanied by cuproptosis could potentially activate adaptive immunity and promote the abscopal effect in tumours outside the radiation field[49]. Indeed, PWCu plus IR treatment significantly increased the infiltration of $CD4^+$ T cells (4.14-fold) and interferon-γ^+ ($IFN\gamma^+$) $CD8^+$ T cells (6.25-fold) in the distant tumour compared to IR alone (Fig. 5h,i and Supplementary Fig. 21). Conversely, αCD8 treatment significantly reduced $CD4^+$ T cell and $IFN\gamma^+$ $CD8^+$ T cell infiltration compared to the combination of PWCu and IR (Fig. 5h,i and Supplementary Fig. 21). These data support the idea that cuproptosis nanocapsules can sensitize acquired radioresistant tumours to radiotherapy and elicit a potent adaptive immune response in distant, non-irradiated tumours.

Enhanced re-irradiation and anti-metastasis by PWCu

Next, a recurrent 4T1 tumour model post-primary irradiation was constructed to evaluate the efficacy of re-irradiation sensitization (Fig. 6a). The 4T1 tumours with a therapeutic starting point of ~200 mm^3 on day 16 were gradually reduced after primary irradiation of 8 Gy × 4 and recurred to ~200 mm^3 on day 36. Prior to re-irradiation, a reconfirmation was obtained regarding the significant up-regulation of FDX1 and LIAS expression in recurrent tumours (Fig. 6b,c). Encouraged by this, we proceeded with the re-irradiation experiment. Interestingly, the combination of PWCu and IR led to an increase in the body weight of

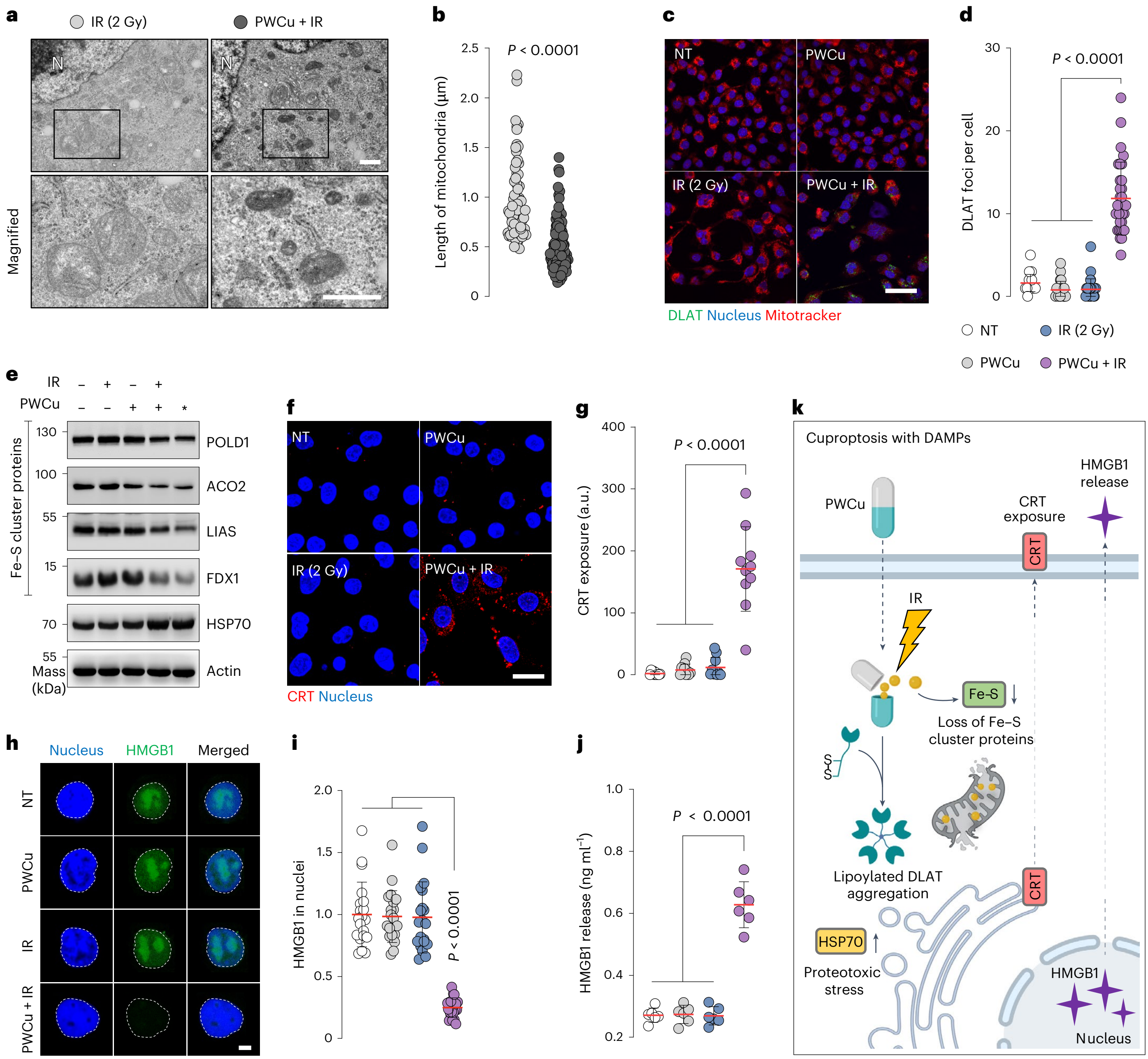

Fig. 4 | Nature of the cell death of dying tumour cells induced by combined PWCu and IR. a, Representative transmission electron microscopy images (scale bars, 1 μm) of 4T1-R cells that were pretreated with or without 10 μM PWCu for 6 h followed by IR irradiation at a dose of 2 Gy. N, nucleus. **b**, The length of mitochondria in **a**; $n \geq 79$ mitochondria. Panels **a** and **b** share colour indication. **c**, Confocal immunofluorescence images (scale bar, 50 μm) of DLAT foci in 4T1-R cells that were pretreated with or without 10 μM PWCu for 6 h followed by IR irradiation at a dose of 2 Gy. **d**, Counts of DLAT foci per cell in **c**; $n = 30$ biologically independent cells. The figure legend (bottom) is shared with **g**, **i** and **j**. **e**, Western blot of cuproptosis-associated proteins in each condition. IR, 2 Gy; *, cuproptosis-positive samples induced by elesclomol–Cu pulse treatment. **f**, Confocal immunofluorescence images (scale bar, 25 μm) of CRT in 4T1-R cells. **g**, Fluorescence intensity of CRT signals in **f**; $n = 10$ biologically independent cells. **h**, Confocal immunofluorescence images (scale bar, 5 μm) of HMGB1 in HCT116-R cells. **i**, Fluorescence intensity of HMGB1 signals per nucleus; $n = 20$ biologically independent cells. **j**, HMGB1 release from HCT116-R cells in each condition quantified by enzyme-linked immunosorbent assay (ELISA); $n = 6$ biologically independent samples. **k**, Scheme of PWCu-triggered cuproptosis accompanied by DAMPs upon IR irradiation. Data in **d**, **g**, **i** and **j** are shown as mean ± s.d. P values were calculated by two-tailed unpaired t-test (**b**) and one-way ANOVA followed by Tukey's multiple comparison test (**d**, **g**, **i** and **j**). The experiments were repeated independently at least two times with similar results. Panel **k** created with BioRender.com.

mice following re-irradiation, while the treatment of IR alone did not (Fig. 6d). This suggests that PWCu plus IR treatment improved the survival quality of mice. Furthermore, local PWCu injection followed by low-dose re-irradiation of 2 Gy × 3 led to significant tumour regression (Fig. 6e and Supplementary Fig. 22). Due to the potent radiosensitizing effect, PWCu plus IR treatment prolonged the median survival time to 90 days, from 56 days for PWCu or IR alone, with complete responses in 40% of mice (Fig. 6f). In addition, PWCu plus IR treatment elicited a robust immune response that significantly inhibited spontaneous lung metastasis, whereas PWCu or IR alone did not (Fig. 6g,h and

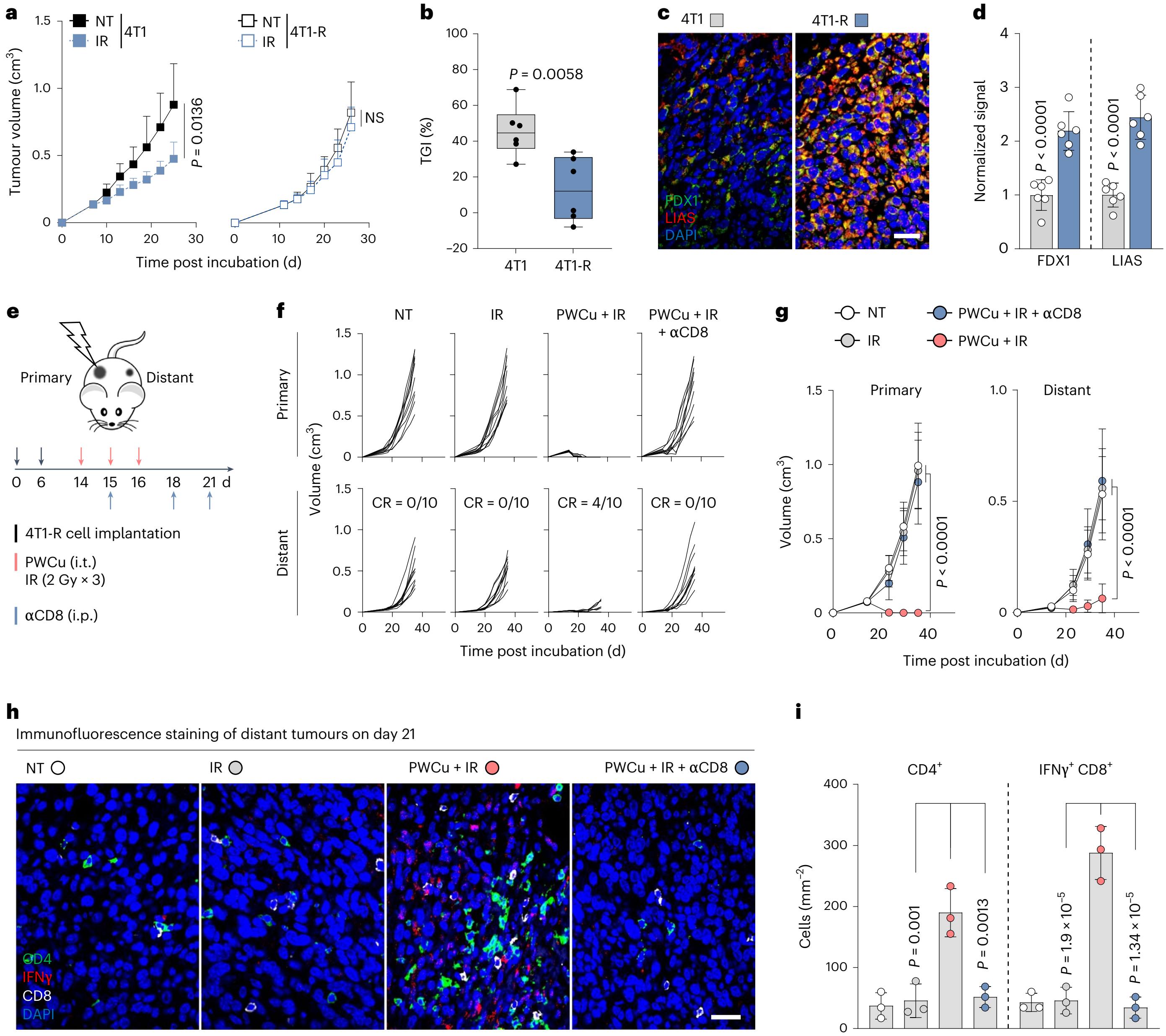

Fig. 5 | Radiosensitization and antitumour immunity mediated by PWCu on radiation-resistant tumours. a, Tumour growth monitored in 4T1 and 4T1-R tumour models irradiated by 2 Gy × 3 IR; $n = 6$ mice; NS, not significant. **b**, Box plots showing tumour growth inhibition (TGI) rates of 2 Gy × 3 IR on 4T1 and 4T1-R tumours; $n = 6$ mice. **c**, Representative confocal images of 4T1 and 4T1-R tumours (scale bar, 25 μm). **d**, Fluorescence intensity of FDX1 and LIAS signals in **c**; $n = 6$ mice. Panels **c** and **d** share colour indication. **e**, Study design of PWCu-mediated radiosensitization on the bilateral flank 4T1-R tumour model. i.t., intratumoural injection; i.p., intraperitoneal injection. **f**,**g**, Tumour growth monitored in the bilateral flank 4T1-R tumour model; $n = 10$ tumours. CR, complete response. **h**, Confocal immunofluorescence images of distant tumour tissues excised on day 21 and stained with the indicated antibodies (scale bar, 25 μm). **i**, Quantitation of CD4$^+$ and IFNγ$^+$ CD8$^+$ T cells in **h**; $n = 3$ tumours. Panels **h** and **i** share colour indication. Data in **a**, **d**, **g** and **i** are represented as mean ± s.d. Data in **b** are represented as box and whiskers (centre line, median; box limits, 25th and 75th percentiles; whiskers, minimum and maximum). *P* values were calculated by two-tailed unpaired *t*-test (**a**, **b** and **d**) and one-way ANOVA followed by Tukey's multiple comparison test (**g** and **i**).

Supplementary Fig. 23). Consistently, PWCu plus IR treatment significantly increased CD8$^+$ cytotoxic T lymphocyte (CTL) infiltration in the pulmonary metastasis compared to PWCu or IR alone (Fig. 6i,j). These results suggest that the cuproptosis nanocapsule can sensitize acquired radiation-resistant tumours to re-irradiation and elicit a robust anti-metastasis immune response.

Discussion

Our data suggest a potential therapeutic target in residual cancer cells with acquired resistance to radiation therapy, which show up-regulation of cuproptosis key regulatory proteins (FDX1 and LIAS), conferring increased susceptibility to cuproptosis. To validate the concept, we synthesized a copper-containing polyoxometalate, PWCu, as a controllable cuproptosis-targeting sensitizer for radiotherapy. IR irradiation facilitates the reduction of Cu^{2+} to Cu$^+$ through reductive radiolysis species such as e^-_{aq}, controlling the release of Cu$^+$ ions from the capsule-like structure of PWCu. In acquired radioresistant cancer cells with increased susceptibility to cuproptosis, these precisely released Cu$^+$ ions activate the intracellular cuproptosis signalling pathway, featured by the aggregation of DLAT and

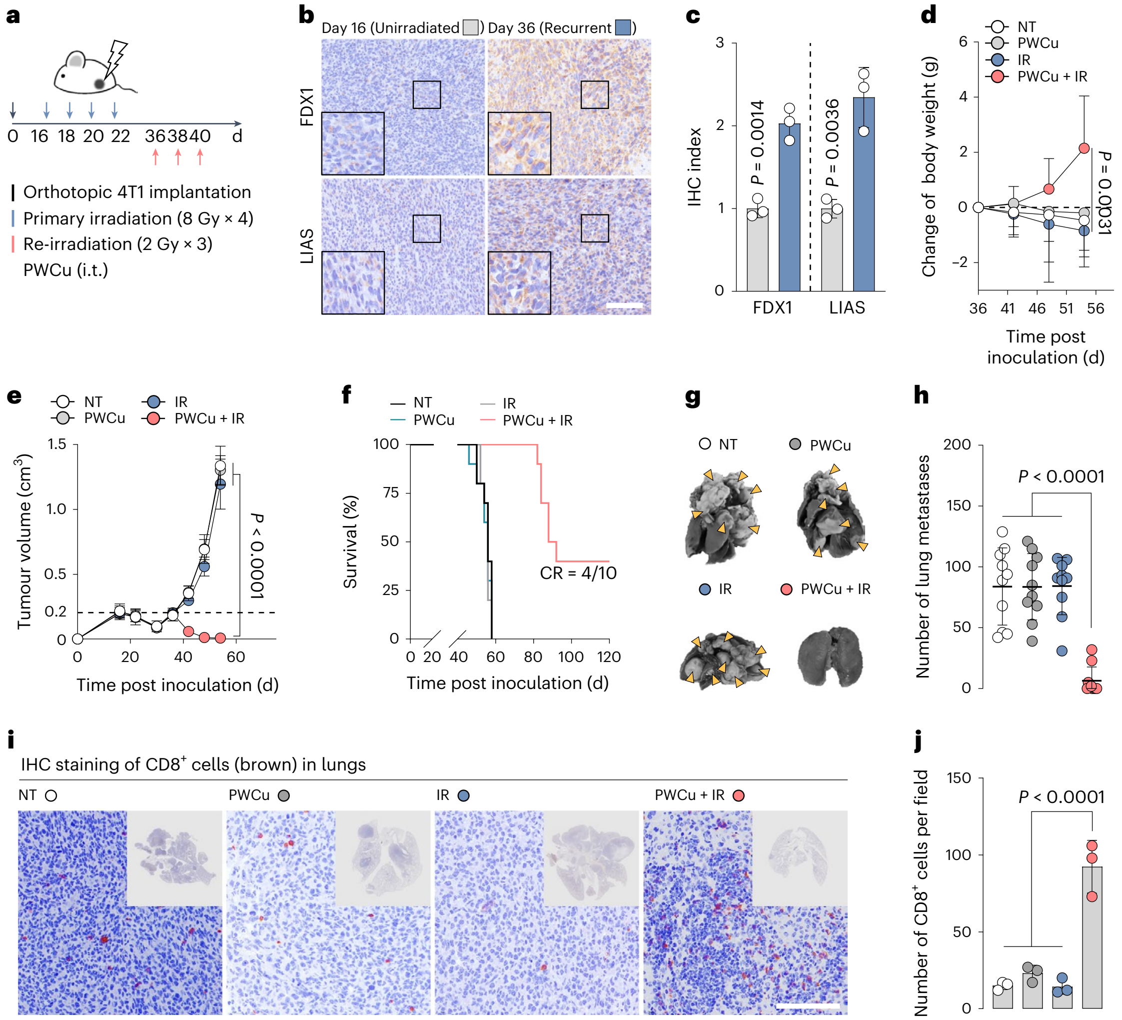

Fig. 6 | Re-irradiation sensitization and anti-metastasis mediated by PWCu. **a**, Treatment scheme of 4T1 tumours in a re-irradiation model. **b**, Representative images (scale bar, 100 μm) of tumour sections stained with FDX1 or LIAS immunohistochemistry (IHC). A zoomed-in view of each boxed region is shown in the lower left insets. **c**, The semiquantitative expression index scored by average optical density value; $n = 3$ fields. Panels **b** and **c** share colour indication. **d**, Body weight change of mice after re-irradiation. **e**, Recurrent tumour growth in different treatment groups as indicated; $n = 10$ mice. **f**, Survival curves for mice. **g**, Representative ex vivo photo of mouse lungs at the endpoint of treatment. The yellow arrows indicate lung metastatic nodules. **h**, Numbers of lung metastatic nodules; $n = 10$ biologically independent samples. Panels **g** and **h** share colour indication. **i**, Representative images (scale bar, 100 μm) of the lung sections stained with CD8⁺ IHC. A full lung slice view is shown in the top right insets. **j**, The count of CD8⁺ cells in each field; $n = 3$ fields. Panels **i** and **j** share colour indication. Data in **c**–**e**, **h** and **j** are shown as mean ± s.d. *P* values were calculated by two-tailed unpaired *t*-test (**c** and **d**) and one-way ANOVA followed by Tukey's multiple comparison test (**e**, **h** and **j**).

down-regulation of Fe–S cluster proteins, thereby inducing tumour cell death due to protein toxicity stress[20]. This cuproptosis-targeting sensitization strategy potently overcomes acquired radioresistance in both acquired radioresistant 4T1-R tumours and recurrent 4T1 tumours after primary radiotherapy.

In clinical practice, managing metastatic tumours effectively is essential for prolonging the survival time of patients[49,50]. While inducing abscopal effects via radiotherapy is beneficial to manage metastatic lesions, the response rate is compromised by radioresistance and low immunogenicity of tumours in patients undergoing re-irradiation[4,51,52]. Notably, our findings demonstrate that PWCu-mediated radiosensitization can effectively trigger immunogenic cuproptosis with increased DAMP levels in the treated tumours and promote CD8⁺ CTL infiltration in untreated distant tumours. Given the immune activation potential of cuproptosis, future research can investigate the potential synergies between cuproptosis-targeting radiotherapy and immunotherapy.

Identification of the cell-death-related features of acquired radioresistant tumours not only advances our preliminary understanding of radioresistance but also provides fresh sensitization perspectives for re-irradiation. Leveraging our preliminary understanding of cuproptosis susceptibility in acquired radioresistant tumours, as elucidated in this study, we showed that the induction of cuproptosis mediated by copper-containing radiosensitizers might be a potent therapeutic strategy for challenging acquired radioresistant tumours, which frequently occur after fractionated radiotherapy. Potentially, our work can facilitate precision radiotherapy with an augmented abscopal effect, thereby improving the re-irradiation outcomes of cancer patients who suffer from metastasis.

Online content

Any methods, additional references, Nature Portfolio reporting summaries, source data, extended data, supplementary information, acknowledgements, peer review information; details of author contributions and competing interests; and statements of data and code availability are available at https://doi.org/10.1038/s41565-024-01784-1.

References

1. Sung, H. et al. Global cancer statistics 2020: GLOBOCAN estimates of incidence and mortality worldwide for 36 cancers in 185 countries. *CA Cancer J. Clin.* **71**, 209–249 (2021).
2. Begg, A. C., Stewart, F. A. & Vens, C. Strategies to improve radiotherapy with targeted drugs. *Nat. Rev. Cancer* **11**, 239–253 (2011).
3. Pitroda, S. P., Chmura, S. J. & Weichselbaum, R. R. Integration of radiotherapy and immunotherapy for treatment of oligometastases. *Lancet Oncol.* **20**, e434–e442 (2019).
4. Nishiga, Y. et al. Radiotherapy in combination with CD47 blockade elicits a macrophage-mediated abscopal effect. *Nat. Cancer* **3**, 1351–1366 (2022).
5. Petroni, G., Cantley, L. C., Santambrogio, L., Formenti, S. C. & Galluzzi, L. Radiotherapy as a tool to elicit clinically actionable signalling pathways in cancer. *Nat. Rev. Clin. Oncol.* **19**, 114–131 (2022).
6. Andratschke, N. et al. European Society for Radiotherapy and Oncology and European Organisation for Research and Treatment of Cancer consensus on re-irradiation: definition, reporting, and clinical decision making. *Lancet Oncol.* **23**, e469–e478 (2022).
7. Fattahi, S. et al. Reirradiation for locoregional recurrent breast cancer. *Adv. Radiat. Oncol.* **6**, 100640 (2021).
8. De Ruysscher, D., Faivre-Finn, C., Le Pechoux, C., Peeters, S. & Belderbos, J. High-dose re-irradiation following radical radiotherapy for non-small-cell lung cancer. *Lancet Oncol.* **15**, e620–e624 (2014).
9. Beddok, A. et al. Clinical and technical challenges of cancer reirradiation: words of wisdom. *Crit. Rev. Oncol. Hematol.* **174**, 103655 (2022).
10. Liu, Y.-P. et al. Endoscopic surgery compared with intensity-modulated radiotherapy in resectable locally recurrent nasopharyngeal carcinoma: a multicentre, open-label, randomised, controlled, phase 3 trial. *Lancet Oncol.* **22**, 381–390 (2021).
11. Xiang, G. et al. Re-irradiation for local primary-recurrence esophageal squamous cell carcinoma treated with IMRT/VMAT. *Radiat. Oncol.* **18**, 114 (2023).
12. Mahantshetty, U. et al. Reirradiation with advanced brachytherapy techniques in recurrent GYN cancers. *Brachytherapy* **22**, 753–760 (2023).
13. Huang, R.-X. & Zhou, P.-K. DNA damage response signaling pathways and targets for radiotherapy sensitization in cancer. *Signal Transduct. Target. Ther.* **5**, 60 (2020).
14. Wang, K. & Tepper, J. E. Radiation therapy-associated toxicity: etiology, management, and prevention. *CA Cancer J. Clin.* **71**, 437–454 (2021).
15. Yang, Y. et al. ZBP1-MLKL necroptotic signaling potentiates radiation-induced antitumor immunity via intratumoral STING pathway activation. *Sci. Adv.* **7**, eabf6290 (2021).
16. Tam, S. Y., Wu, V. W. C. & Law, H. K. W. Influence of autophagy on the efficacy of radiotherapy. *Radiat. Oncol.* **12**, 57 (2017).
17. Lei, G. et al. The role of ferroptosis in ionizing radiation-induced cell death and tumor suppression. *Cell Res.* **30**, 146–162 (2020).
18. Han, C. et al. The AIM2 and NLRP3 inflammasomes trigger IL-1–mediated antitumor effects during radiation. *Sci. Immunol.* **6**, eabc6998 (2021).
19. Chen, H. et al. Radiotherapy modulates tumor cell fate decisions: a review. *Radiat. Oncol.* **17**, 196 (2022).
20. Tsvetkov, P. et al. Copper induces cell death by targeting lipoylated TCA cycle proteins. *Science* **375**, 1254–1261 (2022).
21. Chen, L., Min, J. & Wang, F. Copper homeostasis and cuproptosis in health and disease. *Signal Transduct. Target. Ther.* **7**, 378 (2022).
22. Cobine, P. A. & Brady, D. C. Cuproptosis: cellular and molecular mechanisms underlying copper-induced cell death. *Mol. Cell* **82**, 1786–1787 (2022).
23. Jin, X.-K. et al. Orchestrated copper-based nanoreactor for remodeling tumor microenvironment to amplify cuproptosis-mediated anti-tumor immunity in colorectal cancer. *Mater. Today* **68**, 108–124 (2023).
24. Hasegawa, K., Saga, R. & Hosokawa, Y. Radiotherapeutic review: acquisition of radioresistance and cancer stem cell properties via irradiation. *Radiat. Environ. Med.* **12**, 25–36 (2023).
25. Gray, M. et al. Development and characterisation of acquired radioresistant breast cancer cell lines. *Radiat. Oncol.* **14**, 64 (2019).
26. Zhang, P., et al. Cancer nanomedicine toward clinical translation: obstacles, opportunities, and future prospects. *Med* **4**, 147–167 (2022).
27. Liu, L., Zhao, C., Miller, J. T. & Li, Y. Mechanistic study of CO_2 photoreduction with H_2O on Cu/TiO_2 nanocomposites by in situ X-ray absorption and infrared spectroscopies. *J. Phys. Chem. C* **121**, 490–499 (2017).
28. Wang, D. et al. *In situ* formed Z-scheme graphdiyne heterojunction realizes NIR-photocatalytic oxygen evolution and selective radiosensitization for hypoxic tumors. *ACS Nano* **16**, 21186–21198 (2022).
29. Ding, Z. et al. Radiotherapy reduces *N*-oxides for prodrug activation in tumors. *J. Am. Chem. Soc.* **144**, 9458–9464 (2022).
30. Guo, Z. et al. Radiotherapy-induced cleavage of quaternary ammonium groups activates prodrugs in tumors. *Angew. Chem. Int. Ed.* **61**, e202205014 (2022).
31. Zhang, C. et al. Tumor microenvironment-responsive $Cu_2(OH)PO_4$ nanocrystals for selective and controllable radiosentization via the X-ray-triggered Fenton-like reaction. *Nano Lett.* **19**, 1749–1757 (2019).
32. Wang, L., Jiang, N., Xu, H., Luo, Y. & Zhang, T. Trace Cu(II)-mediated selective oxidation of benzothiazole: the predominance of sequential Cu(II)–Cu(I)–Cu(III) valence transition and dissolved oxygen. *Environ. Sci. Technol.* **57**, 12523–12533 (2023).
33. Zeng, L., Miller, E. W., Pralle, A., Isacoff, E. Y. & Chang, C. J. A selective turn-on fluorescent sensor for imaging copper in living cells. *J. Am. Chem. Soc.* **128**, 10–11 (2006).
34. Liu, X. et al. Actin cytoskeleton vulnerability to disulfide stress mediates disulfidptosis. *Nat. Cell Biol.* **25**, 404–414 (2023).
35. Xu, W. et al. Tumor microenvironment responsive hollow nanoplatform for triple amplification of oxidative stress to enhance cuproptosis-based synergistic cancer therapy. *Adv. Healthc. Mater.* **12**, 2202949 (2023).
36. Zhou, J. et al. Photothermally triggered copper payload release for cuproptosis-promoted cancer synergistic therapy. *Angew. Chem. Int. Ed.* **62**, e202213922 (2023).
37. Guo, B. et al. Cuproptosis induced by ROS responsive nanoparticles with elesclomol and copper combined with αPD-L1 for enhanced cancer immunotherapy. *Adv. Mater.* **35**, 2212267 (2023).
38. Tang, D., Chen, X. & Kroemer, G. Cuproptosis: a copper-triggered modality of mitochondrial cell death. *Cell Res.* **32**, 417–418 (2022).
39. Zhao, B. et al. Photocatalysis-mediated drug-free sustainable cancer therapy using nanocatalyst. *Nat. Commun.* **12**, 1345 (2021).
40. Ning, S. et al. Type-I AIE photosensitizer loaded biomimetic system boosting cuproptosis to inhibit breast cancer metastasis and rechallenge. *ACS Nano* **17**, 10206–10217 (2023).
41. Chan, L. et al. Cuproptosis-driven enhancement of thermotherapy by sequentially response Cu_{2-x}Se via copper chemical transition. *Adv. Funct. Mater.* **33**, 2302054 (2023).

42. Xu, W. et al. A hollow amorphous bimetal organic framework for synergistic cuproptosis/ferroptosis/apoptosis anticancer therapy via disrupting intracellular redox homeostasis and copper/iron metabolisms. *Adv. Funct. Mater.* **32**, 2205013 (2022).
43. Demaria, O. et al. Harnessing innate immunity in cancer therapy. *Nature* **574**, 45–56 (2019).
44. Kroemer, G., Galassi, C., Zitvogel, L. & Galluzzi, L. Immunogenic cell stress and death. *Nat. Immunol.* **23**, 487–500 (2022).
45. Fucikova, J. et al. Detection of immunogenic cell death and its relevance for cancer therapy. *Cell Death Dis.* **11**, 1013 (2020).
46. Liao, Y. et al. Piezoelectric materials for synergistic piezo- and radio-catalytic tumor therapy. *Nano Today* **44**, 101510 (2022).
47. Ni, K. et al. Synergistic checkpoint-blockade and radiotherapy–radiodynamic therapy via an immunomodulatory nanoscale metal–organic framework. *Nat. Biomed. Eng.* **6**, 144–156 (2022).
48. Huang, Z. et al. Nanoscale coordination polymers induce immunogenic cell death by amplifying radiation therapy mediated oxidative stress. *Nat. Commun.* **12**, 145 (2021).
49. Min, Y. et al. Antigen-capturing nanoparticles improve the abscopal effect and cancer immunotherapy. *Nat. Nanotechnol.* **12**, 877–882 (2017).
50. Melo, L. M. N., Lesner, N. P., Sabatier, M., Ubellacker, J. M. & Tasdogan, A. Emerging metabolomic tools to study cancer metastasis. *Trends Cancer* **8**, 988–1001 (2022).
51. Li, H. et al. Nanomedicine embraces cancer radio-immunotherapy: mechanism, design, recent advances, and clinical translation. *Chem. Soc. Rev.* **52**, 47–96 (2023).
52. Twyman-Saint Victor, C. et al. Radiation and dual checkpoint blockade activate non-redundant immune mechanisms in cancer. *Nature* **520**, 373–377 (2015).

Methods

Irradiator settings

A uRT-linac 506c (Shanghai United Imaging Healthcare), Ethos (Varian Medical Systems), TrueBeam (Varian Medical Systems) and Halcyon (Varian Medical Systems) were used for external beam radiation therapy in patients with cervical cancer. The MultiRad 160 irradiator (Precision X-ray) was used for the treatment of solutions, cells and experimental animals. The MultiRad 160 irradiator was set at 160 kV and 15 mA.

Reagents, cell lines and animals

The chemical reagents are listed in Supplementary Table 2. The A549, HeLa, HCT116, MDA-MB-231, 143B, HaCaT, B16-F10, 4T1 and CT26 cell lines were obtained from the Cell Resource Center, Peking Union Medical College. The BEAS-2B (BNCC359274), NCM-460 (BNCC339288) and HK-2 (BNCC339833) cell lines were obtained from the BeNa Culture Collection. The AC16 (CTCC-003-0014), Hepa 1-6 (CTCC-400-0322) and HUVEC (CTCC-0804-PC) cell lines were obtained from Zhejiang Meisen Cell Technology. The radioresistant cell lines 4T1-R, B16-F10-R, A549-R and HCT116-R were obtained through fractionated irradiation. When the cell fusion reached 80%, they were irradiated with 2 Gy and then passaged the next day. This process was repeated for a total of 20 consecutive irradiations. The expression of FDX1 and LIAS proteins was assessed in the radioresistant cell lines 4T1-R, B16-F10-R, A549-R and HCT116-R constructed in this study, as well as in their parental cell lines 4T1, B16-F10, A549 and HCT116, using western blot analysis. C57BL/J, BALB/c and BALB/c-nu female mice (6–8 weeks) were obtained from SPF Biotechnology Co. The tumour volume of mice was calculated using the following formula: $(a \times b^2)/2$, where a is the longest and b is the shortest length. The maximum tumour burden approved was 2 cm^3. The animal study protocol was approved by the Ethics Committee of the Institute of High Energy Physics and Peking Union Medical College Hospital.

Patient samples

Human cervical cancer tissues were collected from eight patients before and after external beam radiation therapy of 1.8 Gy × 20 at Peking Union Medical College Hospital. Permission to use the patient's cervical cancer tissue for this study was approved by the Ethics Committee, Peking Union Medical College Hospital (no. HS-2554). Informed consent was obtained from all participants. The collected tissues were fixed, embedded in 4% paraffin and then subjected to standard immunofluorescence staining after sectioning. Finally, the cells were visualized using a confocal microscope.

Preparation of PWCu nanoclusters

First, 600 g $Na_2WO_4{\cdot}2H_2O$, 740 ml water, 15 ml of 85% H_3PO_4 and 110 ml glacial acetic acid were mixed and stirred. Then, a white precipitate was obtained by filtration. After drying at room temperature, the white powder was dried at 140 °C for 6 h to acquire Δ-$Na_8HPW_9O_{34}{\cdot}19H_2O$ powder. Next, 62 g of $CuCl_2{\cdot}2H_2O$ was dissolved in water (1,200 ml). The pale blue solution was stirred at room temperature while adding 500 g of PW_9 powder until all the PW_9 powder dissolved. Then, 51.5 g NaCl was added to the solution, resulting in the light green solid precipitate. The mixture was stirred for 10 min and heated in hot (60 °C) water until most of the solid precipitate redissolved. The solution was centrifuged for approximately 5 min to remove small blue suspensions. The supernatant was decanted and crystallized at room temperature. The crystals were collected by filtration and washed with ice water. Finally, the PWCu crystals were air-dried at room temperature for subsequent storage and use. The dried PWCu crystals were stored in powder form at room temperature. Prior to use, the stored PWCu powder was reconstituted as a solution and sterilized through a 0.22 μm sterilizing-grade filter membrane.

Radiation-induced Cu^+ release from PWCu

The change in the oxidation state of Cu in solution before and after IR irradiation was detected using a synchrotron-radiation-based XAFS technique. The XAFS spectra of the Cu K edge were measured at the XAFS station of beamline 1W1B of the Beijing Synchrotron Radiation Facility. After irradiation with 0 or 30 Gy of X-rays (MultiRad 160 irradiator), XAFS spectra of the Cu K edge of PWCu-containing PBS solution (50 mg ml^{-1}) were immediately collected. XANES spectra of the Cu K edge were used to analyse the changes in the oxidation state of Cu. CuO and Cu_2O were used as references.

Different concentrations of $CuCl_2$ solution were mixed with the neocuproine reagent, followed by the addition of hydroxylamine hydrochloride. After a 5 min reaction, the absorbance of the mixed solution at 457 nm was detected. The standard curve was constructed by plotting the Cu^+ concentration against the absorbance of neocuproine reagent. The generation of Cu^+ in a PWCu-containing PBS solution (1 mg ml^{-1}) was detected using the neocuproine reagent (final concentration, 0.5 mM) at different radiation doses from 0 to 30 Gy (MultiRad 160, 160 kV, 15 mA). To investigate whether hydrated electrons were involved in the reduction reaction of Cu ions, an electron scavenger KNO_3 (final concentration, 2 mM) or a hydroxyl radical scavenger NaAc (final concentration, 2 mM) was added to the mixed solution of PWCu (final concentration, 0.5 mM) and neocuproine (final concentration, 2.5 mM). After irradiation with 30 Gy, the absorbance was measured.

Coppersensor-1 was used to detect intracellular Cu^+ levels in cells. The 4T1 cells were seeded on confocal laser scanning microscopy dishes at 10×10^4 cells per well. After 12 h, PBS or PWCu (10 μM) was added to the wells and incubated for 6 h. Next, Coppersensor-1 (final dye concentration of 5 μM) was incubated within the dishes followed by X-ray irradiation (4 Gy). The cells were imaged by confocal laser scanning microscopy with 543 nm excitation.

Cell viability assay

To evaluate the susceptibility of the radioresistant cell lines 4T1-R, B16-F10-R, A549-R and HCT116-R, as well as their parental cell lines 4T1, B16-F10, A549 and HCT116, to cuproptosis, elescleomol (30 nM) and $CuCl_2$ (1 μM) were used as inducers of cuproptosis. Cells were plated in 96-well plates. After attachment, the medium containing elescleomol (30 nM) and $CuCl_2$ (1 μM) was added to the wells. After a 2 h incubation, the medium was aspirated and replaced with fresh medium containing $CuCl_2$ (1 μM). The cells were then cultured for an additional 48 h. Subsequently, the medium in each well was replaced with CCK-8 working solution (100 μl) and incubated in a CO_2 incubator for 2 h. Finally, the absorbance at 450 nm in each well was measured using a microplate reader. The cell viability was calculated based on the normalized absorbance. The cuproptosis sensitivity was calculated using the following formula: cuproptosis sensitivity = (1 − cell viability) × 100 (to give a percentage). To evaluate the acute toxicity of PWCu on normal cells including AC16, BEAS-2B, HK-2, HaCaT, HUVEC and NCM-460, cells were seeded at a density of 2,000–5,000 cells per well in 96-well plates. After 12 h, PWCu (0 to 30 μM) was added. After 24 h, a CCK-8 assay was performed. To evaluate the viability of cells treated by PWCu, $CuCl_2$ or PW_9, cells were seeded at a density of 1,000–2,000 cells per well in 96-well plates. After 12 h, cells were pretreated with PWCu, $CuCl_2$ or PW_9 at an equivalent dose (0 to 25 μM) for 6 h and then irradiated by 4 Gy IR. After 60 h, a CCK-8 assay was performed. In the cell death rescue experiments, cell death inducers and protectants were added to the plate after the cells (MDA-MB-231, 143B and HCT116) adhered. Specifically, after adding PWCu for 6 h, a radiation dose of 2 Gy was administered. After 60 h, CCK-8 detection was performed.

Clonogenic assay

The radioresistance of the radioresistant cell lines 4T1-R, B16-F10-R, A549-R and HCT116-R constructed in this study was compared with that of their parental cell lines 4T1, B16-F10, A549 and HCT116 using a clonogenic assay. Cells were plated at a density of 1,000–2,000 cells per well in six-well plates. After the cells adhered, the six-well plates were irradiated with 0, 2, 4, 6 or 8 Gy of X-rays. When colony formation was observed, the cells were fixed with a 4% paraformaldehyde solution and stained with Giemsa stain. To evaluate the radiosensitizing effect, 4T1 cells adhered in the six-well plates (1,000–2,000 cells per well) were preincubated with PBS, $CuCl_2$ (40 μM), PW_9 (20 μM) or PWCu (10 μM) for 6 h, followed by X-ray irradiation (0, 2, 4 or 6 Gy). When colony formation was observed, the cells were fixed with a 4% paraformaldehyde solution and stained with Giemsa stain. In the cell death rescue experiments, 143B, HCT116 or MDA-MB-231 cells adhered in the six-well plates (1,000 cells per well) were preincubated with PWCu (10 μM) and TTM (20 μM), followed by X-ray irradiation (4 Gy). To evaluate the radiosensitizing effect of PWCu on radioresistant cells, B16-F10-R, 4T1-R, A549-R or HCT116-R cells adhered in the six-well plates (1,000–2,000 cells per well) were preincubated with PBS or PWCu (10 μM) for 6 h, followed by X-ray irradiation (0 or 2 Gy). The stained clones were manually counted. The radiation enhancement factor was calculated using methods described in the literature[53]. Specifically, the radiation enhancement factor is the ratio of the radiation dose required to achieve a 10% survival rate.

Transmission electron microscopy assay

Following various treatments, the cells were trypsinized, harvested and subsequently fixed with a 2.5% glutaraldehyde solution, then embedded and sectioned for transmission electron microscopy imaging. The software Nano Measurer v.1.2 was used to measure the length of mitochondria.

Characteristics of cuproptosis

The 4T1-R cells were seeded in the indicated cell plate and incubated with PBS or PWCu (10 μM), followed by IR irradiation (0 or 2 Gy). To observe the aggregation of DLAT, 4T1-R cells treated in each condition were pre-stained with Mitotracker. Afterward, the cells were fixed with 4% paraformaldehyde. Following fixation, standard cell immunofluorescence staining techniques were employed, which involved the use of specific primary antibodies targeting the desired cellular proteins, followed by fluorescently labelled secondary antibodies that bind to the primary antibodies. Finally, the cells were visualized using a confocal microscope. The images were analysed using Fiji (ImageJ v.1.53) or NIS-Elements AR (v.4.51.00) analysis. To examine the Fe–S cluster proteins and HSP70 proteins, the treatment of elesclomol plus $CuCl_2$ was used as a positive inducer for cuproptosis. After various treatments, 4T1-R cells were lysed. During the cell lysis process, proteinase inhibitors and phosphatase inhibitors were added to prevent protein degradation and dephosphorylation. The protein content was then quantified using the Bradford assay. Next, the lysates were mixed with SDS-PAGE sample loading buffer and heated at 90 °C for 10 min to denature the proteins. Following this step, a standard western blotting protocol was initiated.

Immunogenic cell death

The phenomenon of immunogenic cell death was ascertained by the up-regulation of HSP70, the exposure of CRT and the release of HMGB1. The 4T1-R or HCT116-R cells were seeded in the indicated cell plate and incubated with PBS or PWCu (10 μM), followed by IR irradiation (0 and 2 Gy). The HSP70 protein was then examined by western blotting. Next, the 4T1-R or HCT116-R cells were placed in confocal laser scanning microscopy dishes for different treatments and then fixed with paraformaldehyde. Following fixation, standard cell immunofluorescence staining techniques were employed to detect CRT or HMGB1. The images were analysed using Fiji (ImageJ v.1.53) or NIS-Elements AR (v.4.51.00) analysis. The cell culture supernatant of HCT116-R was collected to measure extracellular HMGB1 secretion using an HMGB1 ELISA kit (Elabscience, E-EL-H1554c).

Animal experiments

The orthotopic mouse breast tumour model with or without acquired radiation resistance was set up by injecting 4T1 or 4T1-R cells into the mammary fat pad of BALB/c mice. When tumour volumes reached approximately 130 mm^3, the tumour was subjected to fractionated radiation therapy of 2 Gy per day for a total of three days. Upon reaching a tumour volume of 1,000 mm^3 in the no-treatment group, the mice were subjected to euthanasia, followed by tumour excision, weighing and subsequent sectioning for immunofluorescence staining.

The anti-cancer efficacy of PWCu was tested on the bilateral flank model of 4T1-R tumours. Some 5×10^5 4T1-R cells were subcutaneously implanted onto the right (primary) and left (distant) flanks of BALB/c mice on day 0 and day 6. When the volume of the right tumour reached approximately 75 mm^3, the PWCu solution (500 μg per dose) was directly injected into the primary tumour. After 2 h, the primary tumour received a radiation dose of 2 Gy. The injection and radiation therapy were administered once daily for a total of three doses. For the $CD8^+$ T cell depletion group, on days 15, 18 and 21, mice were intraperitoneally injected with the depletion antibody (anti-CD8, 200 μg per dose). On day 17, some mice were euthanized, and the right-side tumours were dissected out. A portion of the tumours was fixed in a 4% paraformaldehyde solution for subsequent paraffin embedding, sectioning and immunofluorescence staining for FDX1, LIAS, DLAT, HSP70, CRT and HMGB1. Another portion was used for protein extraction for western blot analysis. On day 21, some mice were euthanized, and the left-side tumours were dissected out and fixed in a 4% paraformaldehyde solution for subsequent paraffin embedding, sectioning and immunofluorescence staining for CD8, CD4 and IFNγ. Upon reaching a tumour volume of 1,500 mm^3 in the no-treatment group, the mice were subjected to euthanasia.

The recurrent mouse breast 4T1 tumours after the primary radiation therapy were used to evaluate the re-irradiation sensitizing and anti-metastatic effects of PWCu. Some 5×10^5 4T1 cells were injected into the mammary fat pad of BALB/c mice. When tumour volumes reached approximately 200 mm^3 on day 16, the tumour underwent an initial fractionated radiation therapy of 8 Gy per fraction, with a one-day interval between each fraction (four fractions). When tumour volumes reached approximately 200 mm^3 again on day 36, the tumours were injected with PWCu (500 μg per dose). After 2 h, the tumours underwent a re-irradiation therapy of 2 Gy. The injection and re-irradiation were administered once every two days for a total of three fractions. On days 16 and 36, some mice were euthanized, and the tumours were dissected out and fixed in a 4% paraformaldehyde solution for subsequent paraffin embedding, sectioning and immunohistochemistry staining for FDX1 and LIAS. Mortality was documented in the murine subjects at the earliest of either a tumour volume threshold of 1,500 mm^3 or the time of death. When the mice died or were euthanized, the lungs were dissected out for pathological analysis.

Statistical analysis

Statistical analysis was performed using GraphPad Prism v.9.0.0. For comparisons among multiple groups, one-way ANOVA with Tukey's multiple comparisons post-test was used. For comparisons between two groups, a two-tailed *t*-test was used.

Reporting summary

Further information on research design is available in the Nature Portfolio Reporting Summary linked to this article.

Data availability

All data supporting the findings of this study are included in the paper and its Supplementary Information. Source data are provided with this paper.

References

53. Franken, N. A. P., Rodermond, H. M., Stap, J., Haveman, J. & Van Bree, C. Clonogenic assay of cells in vitro. *Nat. Protoc.* **1**, 2315–2319 (2006).

Acknowledgements

We greatly acknowledge the financial support from the National High Level Hospital Clinical Research Funding (2022-PUMCH-B-052, to F.Z., J.Y. and Z.G.), Strategic Priority Research Program of Chinese Academy of Sciences (XDB36000000, to Z.G.), National Basic Research Program of China (2021YFA1201200 and 2020YFA0710702, to Z.G.), the Directional Institutionalized Scientific Research Project, which relies on the Beijing Synchrotron Radiation Facility of Chinese Academy of Sciences (E12982U810 to Z.G.), the National Natural Science Foundation of China (22375205, to Z.G.) and the Beijing Natural Science Foundation (2222087, to Z.G.).

Author contributions

Y.L. and Z.G. conceived and designed the experiments. Y.L. and D.W. performed the experiments. Y.L. and D.W. synthesized and characterized PWCu polyoxometalates. Y.L. and D.W. performed the cell and animal experiments. C.G., X.W., S.Z. and Z.Z. assisted with the mouse radiation experiment. Y.L., D.W. and Z.G. analysed the data. Y.L. and Z.G. contributed materials and analysis tools. Z.G., J.Y. and F.Z. supervised the project. Y.L., D.W., J.Y. and Z.G. wrote the paper. Y.L. and D.W. revised the paper. All authors discussed the results and edited and approved the paper before submission.

Competing interests

The authors declare no competing interests.

Additional information

Extended data is available for this paper at https://doi.org/10.1038/s41565-024-01784-1.

Supplementary information The online version contains supplementary material available at https://doi.org/10.1038/s41565-024-01784-1.

Correspondence and requests for materials should be addressed to Junfang Yan or Zhanjun Gu.

Peer review information *Nature Nanotechnology* thanks Xin Jiang, Fudi Wang and the other, anonymous, reviewer(s) for their contribution to the peer review of this work.

Reprints and permissions information is available at www.nature.com/reprints.

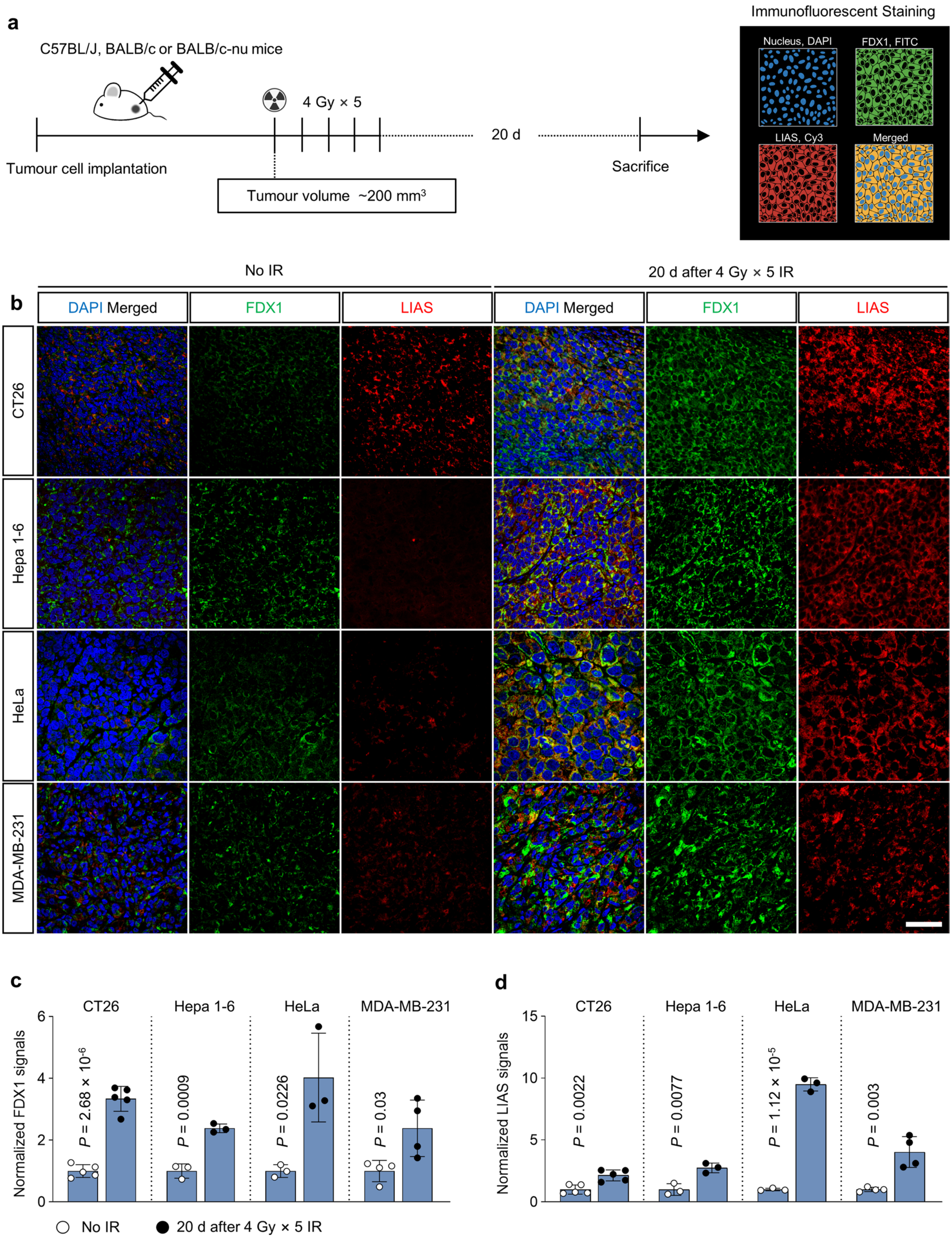

Extended Data Fig. 1 | Up-regulation of FDX1 and LIAS in experimental tumours after EBRT. a, Treatment scheme of tumours from mouse models before and after IR irradiation. **b**, Representative confocal images of tumour lesions before and after IR irradiation (scale bar, 50 μm). **c**, **d**, Normalized fluorescence signals of FDX1 and LIAS (CT26, *n* = 5 mice per group; Hepa 1-6, *n* = 3 mice per group; HeLa, *n* = 3 mice per group; MDA-MB-231, *n* = 4 mice per group). Data in **c**, **d** are shown as mean ± s.d. *P* values were calculated by two-tailed unpaired *t*-test (**c**, **d**). The experiments shown in **b** were repeated independently at least two times with similar results. Panel **a** created with BioRender.com.

https://doi.org/10.1038/s41565-024-01784-1

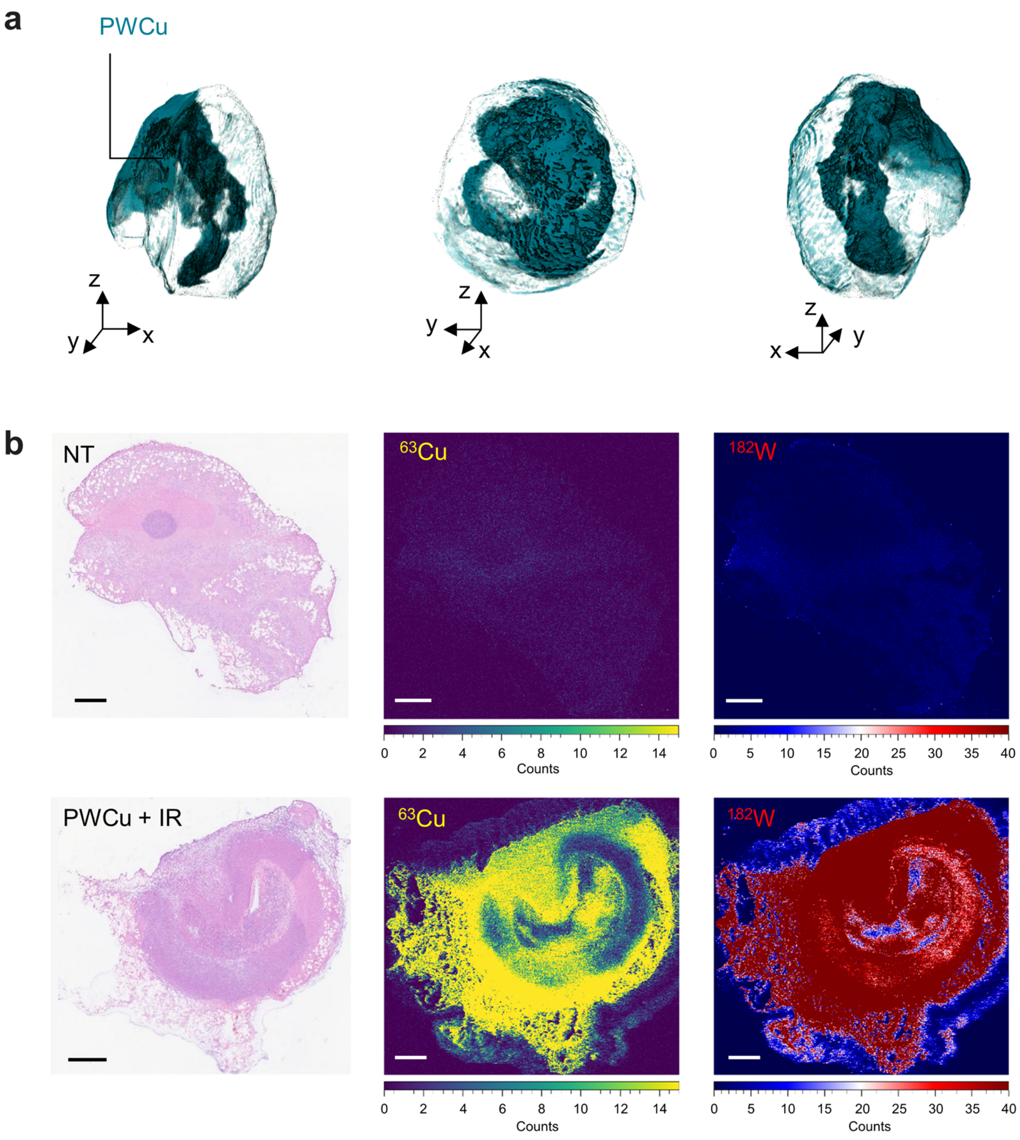

Extended Data Fig. 2 | The intratumoral distribution of PWCu after intratumoral injection. **a**, 3D reconstruction images of synchrotron radiation micro-CT. **b**, H&E staining images (scale bar, 500 µm) and LA-ICP-TOFMS element mapping images (scale bar, 500 µm) of tumour tissue. LA-ICP-TOFMS, laser ablation-inductively coupled plasma-time of flight mass spectrometry. The experiments in **b** were repeated independently at least two times with similar results.

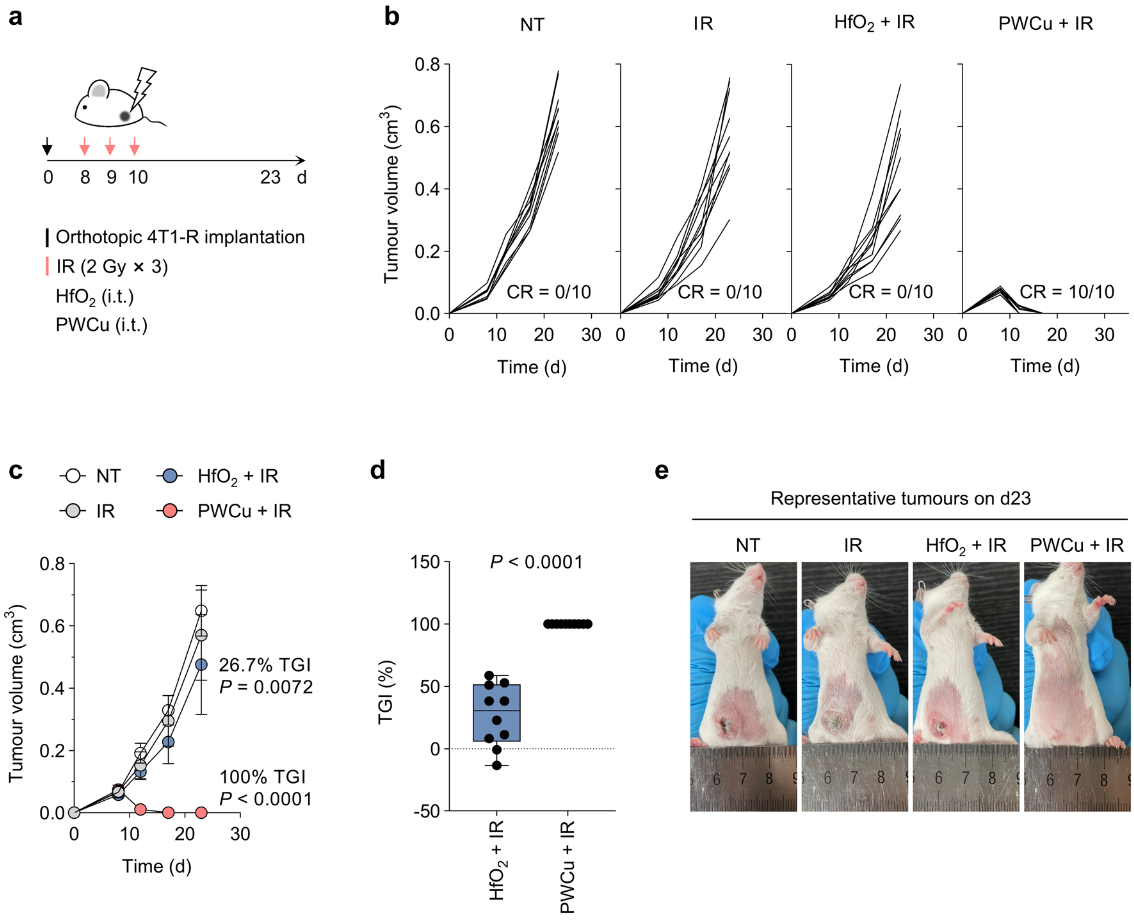

Extended Data Fig. 3 | Comparison of radiosensitizing effect between HfO_2 and PWCu. **a**, Schematic diagram of orthotopic 4T1-R breast cancer establishment and radiotherapy. **b**, **c**, Growth curves of tumours. Results are expressed as mean tumour volume ± s.d. with % TGI and *P* value relative to NT (on day 23) as determined by two-tailed unpaired *t*-test. *n* = 10 biologically independent mice per group. CR, complete response. **d**, Tumour growth inhibition rates of 2 Gy × 3 IR on 4T1-R tumours. *n* = 10 biologically independent mice per group. **e**, Representative photographs of tumours. Data in **d** are represented as box and whiskers (centre line, median; box limits, 25th and 75th percentiles; whiskers, minimum and maximum). The *P* value was calculated by two-tailed unpaired *t*-test (**d**).

nature portfolio

Corresponding author(s): Zhanjun Gu

Last updated by author(s): Jul 18, 2024

Reporting Summary

Nature Portfolio wishes to improve the reproducibility of the work that we publish. This form provides structure for consistency and transparency in reporting. For further information on Nature Portfolio policies, see our Editorial Policies and the Editorial Policy Checklist.

Statistics

For all statistical analyses, confirm that the following items are present in the figure legend, table legend, main text, or Methods section.

n/a	Confirmed	
☐	☒	The exact sample size (*n*) for each experimental group/condition, given as a discrete number and unit of measurement
☐	☒	A statement on whether measurements were taken from distinct samples or whether the same sample was measured repeatedly
☐	☒	The statistical test(s) used AND whether they are one- or two-sided *Only common tests should be described solely by name; describe more complex techniques in the Methods section.*
☒	☐	A description of all covariates tested
☐	☒	A description of any assumptions or corrections, such as tests of normality and adjustment for multiple comparisons
☐	☒	A full description of the statistical parameters including central tendency (e.g. means) or other basic estimates (e.g. regression coefficient) AND variation (e.g. standard deviation) or associated estimates of uncertainty (e.g. confidence intervals)
☐	☒	For null hypothesis testing, the test statistic (e.g. *F*, *t*, *r*) with confidence intervals, effect sizes, degrees of freedom and *P* value noted *Give P values as exact values whenever suitable.*
☒	☐	For Bayesian analysis, information on the choice of priors and Markov chain Monte Carlo settings
☒	☐	For hierarchical and complex designs, identification of the appropriate level for tests and full reporting of outcomes
☒	☐	Estimates of effect sizes (e.g. Cohen's *d*, Pearson's *r*), indicating how they were calculated

Our web collection on statistics for biologists contains articles on many of the points above.

Software and code

Policy information about availability of computer code

Data collection	Nikon A1 was used to collect the confocal images. Azure Biosystems C300 was used to collect western blotting images. RIGAKU XtaLAB Synergy-S X-ray single crystal diffractometer was used to collect single crystal diffraction data. Malvern Zetasizer Nano ZS90 was used to collect the size data. Thermo Scientific K-Alpha was used to detect X-ray photoelectron spectroscopy spectra. The XAFS station of beamline 1W1B of Beijing Synchrotron Radiation Facility was used to collect the XAFS spectra of Cu K-edge. The absorbance of the solution was detected by Agilent Cary 5000, Thermo Multiskan MK3, or TECAN Infinite M200 Pro. Flow cytometry data were acquired by using Beckman CytoFLEX S. Hitachi HT7800 was used to collect the bio-TEM images. The Seahorse XFe96 Analyzer was used to measure the oxygen consumption rate of live cells. Hitachi 7100 automatic biochemical analyzer was used to collect serum biochemical parameters. Mindray BC-2800Vet was used to collect hematological parameters. The 2D elemental distribution in tumour tissue slices was collected by using LA-ICP-TOFMS system with a Laser Ablation System (Iridia Bio, Teledyne Photon Machines) and an Inductively Coupled Plasma Time-of-Flight Mass Spectrometry system (icpTOF 2R, TOFWERK). The µCT station of beamline 4W1A of Beijing Synchrotron Radiation Facility was used to collect the µCT images. Thermo-X7 was used to collect the content of Cu element in tumor, blood, and main tissues. Tissue staining data were collected using 3DHISTECH Panoramic DESK or OLYMPUS IX73.
Data analysis	GraphPad Prism (v9.0.0) was used for plotting and statistical analysis. Nano Measurer (v1.2) was used to measure the length of mitochondria in Bio-TEM images. CytExpert (v2.4) was used for analysis of flow cytometry data. Fiji (ImageJ v1.53) was used for image analysis. The BSRF in-house software MOCUPY (v1.0) based on CUDA Python (v3.8) was used as the pre-processing algorithm to reconstruct the 3D tomographic data. Avizo software (v2019.1) was used for the 3D volumetric visualization of µCT data.

For manuscripts utilizing custom algorithms or software that are central to the research but not yet described in published literature, software must be made available to editors and reviewers. We strongly encourage code deposition in a community repository (e.g. GitHub). See the Nature Portfolio guidelines for submitting code & software for further information.

Data

Policy information about availability of data

All manuscripts must include a data availability statement. This statement should provide the following information, where applicable:

- Accession codes, unique identifiers, or web links for publicly available datasets
- A description of any restrictions on data availability
- For clinical datasets or third party data, please ensure that the statement adheres to our policy

All data supporting the findings of this study are included in the paper and its Supplementary Information. Source Data are provided with this paper.

Research involving human participants, their data, or biological material

Policy information about studies with human participants or human data. See also policy information about sex, gender (identity/presentation), and sexual orientation and race, ethnicity and racism.

Reporting on sex and gender	There were 8 cervical cancer patients participated in this study after signing the informed consent form, who were determined as female by self-reporting. The study investigators of Beijing Union Medical College Hospital collected cervical cancer tissue samples for this study in an approved and reasonable manner.
Reporting on race, ethnicity, or other socially relevant groupings	N/A
Population characteristics	No data on population characteristics was collected.
Recruitment	The study investigators of Beijing Union Medical College Hospital identified and recruited participants according to the study eligibility.
Ethics oversight	The study protocol was approved by the Ethics Committee of Beijing Union Medical College Hospital (No. HS-2554).

Note that full information on the approval of the study protocol must also be provided in the manuscript.

Field-specific reporting

Please select the one below that is the best fit for your research. If you are not sure, read the appropriate sections before making your selection.

☒ Life sciences ☐ Behavioural & social sciences ☐ Ecological, evolutionary & environmental sciences

For a reference copy of the document with all sections, see nature.com/documents/nr-reporting-summary-flat.pdf

Life sciences study design

All studies must disclose on these points even when the disclosure is negative.

Sample size	No statistical methods were used to predetermine the sample sizes. It is impossible to predict the magnitude of experimental variation between animals based on our current knowledge. Sample size was chosen to ensure reproducibility of the experiments in accordance with the replacement, reduction and refinement principles of animal ethics regulation. The sample sizes reported in the present study are comparable to those used in previous and similar publications. The group sizes (at least three animals per treatment group) represents the minimum number animals needed to reach statistical significance ($p < 0.05$) between experimental groups.
Data exclusions	No exclusion method was used in this study.
Replication	Experiments results were robust and reproducible. Experiments were performed at least twice. Replication of experiments was noted in the figure caption.
Randomization	All samples and mice were randomly assigned into groups.
Blinding	No blinding was done in this study. Most of the studies contained multiple steps (including the material preparation, mouse tumour treatment, and so on) and the scientists must keep careful track of conditions. All experimental analyses were done objectively and did not require blinding.

Reporting for specific materials, systems and methods

We require information from authors about some types of materials, experimental systems and methods used in many studies. Here, indicate whether each material, system or method listed is relevant to your study. If you are not sure if a list item applies to your research, read the appropriate section before selecting a response.

Materials & experimental systems

n/a	Involved in the study	
☐	☒	Antibodies
☐	☒	Eukaryotic cell lines
☒	☐	Palaeontology and archaeology
☐	☒	Animals and other organisms
☒	☐	Clinical data
☒	☐	Dual use research of concern
☒	☐	Plants

Methods

n/a	Involved in the study	
☒	☐	ChIP-seq
☐	☒	Flow cytometry
☒	☐	MRI-based neuroimaging

Antibodies

Antibodies used

Antibody (Catalog number/description); Provider; Dilution used.
Antibodies for immunofluorescence and immunohistochemistry:
Rabbit anti-FDX1 (ab108257); Abcam; 1 to 200.
Rabbit anti-LIAS (11577-1-AP); Proteintech; 1 to 200.
Mouse anti-DLAT (YM1328); Immunoway; 1 to 300.
Rabbit anti-CRT (#12238); Cell Signaling Technology; 1 to 200.
Rabbit anti-CRT (GB112134-100); Servicebio; 1 to 250.
Rabbit anti-HMGB1 (ab79823); Abcam; 1 to 250.
Rabbit anti-HMGB1 (GB11103-100); Servicebio; 1 to 300.
Rabbit anti-CD4 (GB15064-100); Servicebio; 1 to 200.
Rabbit anti-CD8 (GB114196-100); Servicebio; 1 to 500.
Mouse anti-IFN-γ (YT2279); Immunoway; 1 to 200.
Mouse anti-HSP70 (GB15241-100); Servicebio; 1 to 500.
Alexa Fluor® 488-conjugated Goat Anti-Rabbit IgG (H+L) (GB25303); Servicebio; 1 to 200.
HRP conjugated Goat Anti-Rabbit IgG (H+L) (GB23303); Servicebio; 1 to 200.
Antibodies for Western Blot:
Rabbit anti-FDX1 (ab108257); Abcam; 1 to 1000.
Rabbit anti-LIAS (11577-1-AP); Proteintech; 1 to 2500.
Rabbit anti-Lipoic Acid (ab58724); Abcam; 1 to 1000.
Rabbit anti-POLD1 (ab186407); Abcam; 1 to 1000.
Rabbit anti-ACO2 (ab129069); Abcam; 1 to 2000.
Rabbit anti-HSP70 (ab5439); Abcam; 1 to 1000.
Rabbit anti-ACTIN (AF5003); Beyotime; 1 to 1000.
HRP-labeled Goat Anti-Rabbit IgG(H+L) (A0208); Beyotime; 1 to 1000.
Antibody for in vivo cell depletion:
Ultra-LEAF™ Purified anti-mouse CD8a Antibody (100763); Biolegend.

Validation

All antibodies were validated by literatures and/or by the respective manufacturers.
1. Rabbit anti-FDX1 (ab108257) has been validated for WB analysis by the manufacturer. Rabbit anti-FDX1 (ab108257) has been validated for IHC analysis by the literature (Tsvetkov et al., Science 375, 1254–1261 (2022)). Reactivity with human, mouse and rat was tested. https://www.abcam.cn/products/primary-antibodies/adx-antibody-epr4629-ab108257.html.
2. Rabbit anti-LIAS (11577-1-AP) has been validated for WB and IHC analysis by the manufacturer. Reactivity with human, mouse and rat was tested. https://www.ptgcn.com/products/LIAS-Antibody-11577-1-AP.htm#publications.
3. Mouse anti-DLAT (YM1328) has been validated for IF analysis by the manufacturer. Reactivity with human and mouse was tested. http://www.immunoway.com/Home/22/YM1328.
4. Rabbit anti-CRT (#12238) has been validated for IF analysis by the manufacturer. Reactivity with human, mouse and rat was tested. https://www.cellsignal.cn/products/primary-antibodies/calreticulin-d3e6-xp-rabbit-mab/12238.
5. Rabbit anti-CRT (GB112134-100) has been validated for IF analysis by the manufacturer. Reactivity with human, mouse and rat was tested. https://www.servicebio.cn/goodsdetail?id=5108.
6. Rabbit anti-HMGB1 (ab79823) has been validated for IF analysis by the manufacturer. Reactivity with human, mouse and rat was tested. https://www.abcam.cn/products/primary-antibodies/hmgb1-antibody-epr3507-ab79823.html.
7. Rabbit anti-HMGB1 (GB11103-100) has been validated for IF analysis by the manufacturer. Reactivity with human, mouse and rat was tested. https://www.servicebio.cn/goodsdetail?id=1383.
8. Rabbit anti-CD4 (GB15064-100) has been validated for IF analysis by the manufacturer. Reactivity with mouse were tested. https://www.servicebio.cn/goodsdetail?id=13685.
9. Rabbit anti-CD8 (GB114196-100) has been validated for IHC and IF analysis by the manufacturer. Reactivity with mouse was tested. https://www.servicebio.cn/goodsdetail?id=11280.
10. Mouse anti-IFN-γ (YT2279) has been validated for IF analysis by the manufacturer. Reactivity with human, mouse and rat was tested. http://www.immunoway.com/Home/22/YT2279.
11. Mouse anti-HSP70 (GB15241-100) has been validated for IF analysis by the manufacturer. Reactivity with human, mouse and rat was tested. https://www.servicebio.cn/goodsdetail?id=14866.
12. Rabbit anti-Lipoic Acid (ab58724) has been validated for WB analysis by the manufacturer. Reactivity with species independent was tested. https://www.abcam.cn/products/primary-antibodies/lipoic-acid-antibody-ab58724.html.
13. Rabbit anti-POLD1 (ab186407) has been validated for WB analysis by the manufacturer. Reactivity with human, mouse and rat was tested. https://www.abcam.cn/products/primary-antibodies/pold1-antibody-epr15118-ab186407.html.
14. Rabbit anti-ACO2 (ab129069) has been validated for WB analysis by the manufacturer. Reactivity with human was tested. https://www.abcam.cn/products/primary-antibodies/aconitase-2-antibody-epr8282b-ab129069.html.

15. Rabbit anti-HSP70 (ab5439) has been validated for WB analysis by the manufacturer. Reactivity with human, mouse and rat was tested. https://www.abcam.cn/products/primary-antibodies/hsp70-antibody-3a3-ab5439.html.
16. Rabbit anti-ACTIN (AF5003) has been validated for WB analysis by the manufacturer. Reactivity with human, mouse and rat was tested. https://www.beyotime.com/product/AF5003.htm.
17. Ultra-LEAF™ Purified anti-mouse CD8a Antibody (100763) has been validated for depletion application in the literature (Wang Y, et al. 2021. Nat Commun. 12:4964.). Reactivity with mouse was tested. https://www.biolegend.com/en-us/products/ultra-leaf-purified-anti-mouse-cd8a-antibody-7731.

Eukaryotic cell lines

Policy information about cell lines and Sex and Gender in Research

Cell line source(s)	A549, HeLa, HCT116, MDA-MB-231, 143B, HaCaT, B16F10, 4T1, and CT26 cell lines were obtained from the Cell Resource Center, Peking Union Medical College. BEAS-2B (BNCC359274), NCM-460 (BNCC339288), and HK-2 (BNCC339833) cell lines were obtained from BeNa Culture Collection. AC16 (CTCC-003-0014), Hepa1-6 (CTCC-400-0322), and HUVEC (CTCC-0804-PC) cell lines were obtained from Zhejiang Meisen Cell Technology Co., LTD.
Authentication	Identity of the cell lines were frequently checked by their morphological features and they were authenticated by the short tandem repeat (STR) profiling initially.
Mycoplasma contamination	Cells were regularly tested and confirmed without mycoplasma contamination.
Commonly misidentified lines (See ICLAC register)	No commonly misidentified cell lines are used in this study.

Animals and other research organisms

Policy information about studies involving animals; ARRIVE guidelines recommended for reporting animal research, and Sex and Gender in Research

Laboratory animals	6-8 week-old C57BL/J, BALB/c or BALB/c-nu female mice were used for animal experiments described in this study. Mice were kept with free access to standard food and water. All care and handling of animals were performed with the approval of the Ethics Committee of Institute of High Energy Physics and Peking Union Medical College Hospital. Animals were housed at a density of 4–5 mice per cage, maintained at a temperature of ~25 °C in a humidity-controlled environment with a 12 h light/dark cycle.
Wild animals	The study did not involve wild animals.
Reporting on sex	All mice used in this study were female.
Field-collected samples	The study did not involve samples collected from the field.
Ethics oversight	All animal experiments were performed in accordance with the guidelines approved by the Ethics Committee of Institute of High Energy Physics and Peking Union Medical College Hospital.

Note that full information on the approval of the study protocol must also be provided in the manuscript.

Plants

Seed stocks	*Report on the source of all seed stocks or other plant material used. If applicable, state the seed stock centre and catalogue number. If plant specimens were collected from the field, describe the collection location, date and sampling procedures.*
Novel plant genotypes	*Describe the methods by which all novel plant genotypes were produced. This includes those generated by transgenic approaches, gene editing, chemical/radiation-based mutagenesis and hybridization. For transgenic lines, describe the transformation method, the number of independent lines analyzed and the generation upon which experiments were performed. For gene-edited lines, describe the editor used, the endogenous sequence targeted for editing, the targeting guide RNA sequence (if applicable) and how the editor was applied.*
Authentication	*Describe any authentication procedures for each seed stock used or novel genotype generated. Describe any experiments used to assess the effect of a mutation and, where applicable, how potential secondary effects (e.g. second site T-DNA insertions, mosiacism, off-target gene editing) were examined.*

Flow Cytometry

Plots

Confirm that:

☒ The axis labels state the marker and fluorochrome used (e.g. CD4-FITC).

☒ The axis scales are clearly visible. Include numbers along axes only for bottom left plot of group (a 'group' is an analysis of identical markers).

☒ All plots are contour plots with outliers or pseudocolor plots.

☒ A numerical value for number of cells or percentage (with statistics) is provided.

Methodology

Sample preparation	Cells were trypsinized, harvested and washed with PBS and then analysed with flow cytometer. Cells were stained with probes according to the manufacturer's protocols, and then analyzed by flow cytometry.
Instrument	Beckman CytoFLEX S
Software	CytExpert v2.4
Cell population abundance	Each experiment involved only one type of cell lines and no sorting was performed. 20000 events were collected in each analysis.
Gating strategy	In general, cells were gated on FSC-A/SSC-A. The fluorescence signal of the TMRE probe in the single cell population was analyzed.

☒ Tick this box to confirm that a figure exemplifying the gating strategy is provided in the Supplementary Information.